Lower urban humidity moderates heat stress

TC Chakraborty[1], Zander Venter[2], Yun Qian[3], and Xuhui Lee[4]

[1]Pacific Northwest National lab
[2]Norwegian Institute for Nature Research
[3]Pacific Northwest National Laboratory (DOE)
[4]Yale University, School of Forestry and Environmental Studies

November 28, 2022

Abstract

Radiative skin temperature is often used to examine heat exposure in multi-city studies and for informing urban heat management efforts since urban air temperature is rarely measured at the appropriate scales. Cities also have lower relative humidity, which is not traditionally accounted for in large-scale observational urban heat risk assessments. Here using crowdsourced measurements from over 40,000 weather stations in [?]600 urban clusters in Europe, we show the moderating effect of this urbanization-induced humidity reduction on heat stress during the 2019 heatwave. We demonstrate that daytime differences in heat index between urban clusters and their surroundings are weak and associations of this urban-rural difference with background climate, generally examined from the skin temperature perspective, is diminished due to moisture feedback. We also examine the spatial variability of skin temperature, air temperature, and heat indices within these clusters, relevant for detecting hotspots and potential disparities in heat exposure, and find that skin temperature is a poor proxy for the intra-urban distribution of heat stress. Finally, urban vegetation shows much weaker (~1/6$^{\text{th}}$ as strong) associations with heat stress than with skin temperature, which has broad implications for optimizing urban heat mitigation strategies. Our results are valid for both operational metrics of heat stress (such as apparent temperature and Humidex) and for various empirical heat indices from epidemiological studies. This study provide large-scale empirical evidence that skin temperature, used due to the lack of better alternatives, is weakly suitable for informing heat mitigation strategies within and across cities, necessitating more urban meteorological observations.

Hosted file

`draft_submit.docx` available at https://authorea.com/users/538595/articles/606943-lower-urban-humidity-moderates-heat-stress

Lower urban humidity moderates heat stress

T. Chakraborty[1,3,*], Z. S. Venter[2], Y. Qian[3], X. Lee[1,*]

[1]School of the Environment, Yale University, New Haven, CT, USA

[2]Terrestrial Ecology Section, Norwegian Institute for Nature Research—NINA, 0349 Oslo, Norway

[3]Pacific Northwest National Laboratory, Richland, WA, USA

Key Points

- Lower humidity and higher air temperature in cities compared to rural backgrounds compensate for each other to moderate heat stress
- Radiative skin temperature is a poor proxy for both intra-urban heterogeneity and variability in urban-rural difference in heat stress
- Vegetation is much less efficient at reducing heat stress than at reducing satellite-derived skin temperature

Key words: Heat stress; urban climate; humidity; crowdsourced data; remote sensing; urban vegetation

*Corresponding authors: T. Chakraborty (tc.chakraborty@pnnl.gov) and X. Lee (xuhui.lee@yale.edu)

Abstract

Radiative skin temperature is often used to examine heat exposure in multi-city studies and for informing urban heat management efforts since urban air temperature is rarely measured at the appropriate scales. Cities also have lower relative humidity, which is not traditionally accounted for in large-scale observational urban heat risk assessments. Here using crowdsourced measurements from over 40,000 weather stations in ≈600 urban clusters in Europe, we show the moderating effect of this urbanization-induced humidity reduction on heat stress during the 2019 heatwave. We demonstrate that daytime differences in heat index between urban clusters and their surroundings are weak and associations of this urban-rural difference with background climate, generally examined from the skin temperature perspective, is diminished due to moisture feedback. We also examine the spatial variability of skin temperature, air temperature, and heat indices within these clusters, relevant for detecting hotspots and potential disparities in heat exposure, and find that skin temperature is a poor proxy for the intra-urban distribution of heat stress. Finally, urban vegetation shows much weaker (~1/6th as strong) associations with heat stress than with skin temperature, which has broad implications for optimizing urban heat mitigation strategies. Our results are valid for both operational metrics of heat stress (such as apparent temperature and Humidex) and for various empirical heat indices from epidemiological studies. This study provide large-scale empirical evidence that skin temperature, used due to the lack of better alternatives, is weakly suitable for informing heat mitigation strategies within and across cities, necessitating more urban meteorological observations.

Plain Language Summary

A central theme in urban climatology is that cities have higher heat stress than their background rural landscapes. In scientific studies across many cities, satellite observations are often used as a proxy for this higher urban heat stress. However, satellites measure the temperature of the urban surface, while heat stress is mainly a function of air temperature and humidity. It is critical to know how well, if at all, satellites capture urban heat stress, which has been traditionally difficult to measure using ground observations due to the lack of weather stations in cities. Here, we use measurements from over 40,000 citizen weather stations over Europe to address this important gap and compare the distributions of satellite-derived surface temperature, air temperature, and heat stress during the July 2019 heatwave. We find that the lower relative humidity due to urbanization partly offsets the effect of higher air temperatures on urban heat stress. Moreover, satellite-derived surface temperature shows very weak relationships with air temperature and heat stress, both within cities and when examining urban-rural differences across cities. Finally, urban vegetation is much less effective at reducing heat stress than at reducing surface temperature. These results are relevant for informing future urban research.

1. Introduction

As the world continues to warm, with heatwaves becoming more frequent and intense (Perkins-Kirkpatrick & Lewis, 2020), urban areas are expected to face the brunt of the impacts due to large populations and higher temperatures (Heaviside et al., 2017; Heilig, 2014). That cities, on average, have higher temperatures than their surroundings – the urban heat island (UHI) effect – is well-established (Arnfield, 2003; Qian et al., 2022). However, the time and magnitude of this phenomenon varies substantially across cities and depends on the type of temperature measurement (Ho et al., 2016; Venter et al., 2021; Zhang et al., 2014). Even though UHI estimates were traditionally from air temperature (T_a) measurements (Howard, 1833), many recent large-scale observational and modeling studies on the UHI, and urban climate in general, have focused on radiative skin temperature (T_s) (Chakraborty et al., 2019; Chakraborty & Lee, 2019; Clinton & Gong, 2013; Hoffman et al., 2020; Hsu et al., 2021; Manoli et al., 2019; Mentaschi et al., 2022; Schwaab et al., 2021; L. Zhao et al., 2014, 2017), with many of these studies commenting on heat exposure in cities, their public health consequences, and potential mitigation strategies. Similarly, maps derived from T_s are often used as a guide for planning heat mitigation strategies by decision makers (Keith et al., 2019). However, T_a is more relevant for heat exposure than T_s, but is difficult to measure in cities due to the dearth of standard weather stations and hard to model due to multiple confounding factors (Ho et al., 2016; Muller et al., 2013; Stone Jr et al., 2019). The two variables – T_a and T_s – are physically distinct (Jin & Dickinson, 2010), and the urban-rural differences in T_a (ΔT_a) and T_s (ΔT_s) are also not well correlated (Venter et al., 2021; Zhang et al., 2014), which brings into question the potential public health and policy implications of urban studies using T_s.

Urban areas may also be drier than their surroundings (particularly in humid climate) due to the removal of vegetation and pervious surfaces - the urban dry island (UDI) effect (Lokoshchenko, 2017; Qian et al., 2022). In comparison to the multitude of studies on the UHI, the UDI is rarely considered in large-scale urban heat risk assessments due to the lack of consensus on a standard metric for urban moisture content (Z. Wang et al., 2021) and the difficulty in measuring near-surface moisture within cities, even when using satellites. The human physiological response to heat depends not just on T_a, but also on relative humidity (RH) (Anderson et al., 2013; Raymond et al., 2020; Sherwood & Huber, 2010). Electricity demand for cooling buildings, expected to be enhanced due to the UHI, also depends on atmospheric humidity (Maia-Silva et al., 2020). Therefore, a more accurate understanding of the impact of urbanization on public health, energy demand, and the economy should account for the combined impacts of T_a and RH. Although modeling studies have the freedom to examine simulated T_a and RH (and thus, heat stress) over urban areas (Huang et al., 2021; Oleson et al., 2015; Sarangi et al., 2021; L. Zhao et al., 2021), models use simplified representations of urban areas with multiple sources of uncertainty (Krayenhoff et al., 2021; Qian et al., 2022; Sharma et al., 2021; Zheng et al., 2021). Additionally, it is computationally expensive to run such models at fine-enough scales to resolve intra-urban variability.

Here we combine dense citizen weather station (CWS) measurements and satellite observations over Europe during the July 2019 heatwave to comprehensively examine the distributions of T_s, T_a, RH, and heat stress within and across satellite-derived urban clusters. We consider several metrics, both empirical and thermodynamic, for estimating heat stress, including the apparent temperature used by the US National Weather Service (HI_0), which describes what the temperature feels like to humans when humidity is accounted for (Rothfusz, 1990; Steadman, 1979). Our results, based on measurements from over 40,000 (after quality control) CWSs in over 600 clusters, suggest that the lower RH in these cities partially cancels out the impact of higher T_a on heat stress during daytime, resulting in smaller differences in HI_0 (and several other heat indices considered) between urban areas and their surroundings. We also analyze the spatial gradients of these variables within clusters and demonstrate that satellite-derived T_s poorly captures the spatial distribution of ambient HI_0 within cities. Finally, with reference to the notion of employing urban vegetation to reduce local-scale heat stress, we find that vegetation is much less efficient at lowering HI_0 than lowering T_s at these scales. These results demonstrate the contrasting roles T_a and RH play to moderate urbanization-induced heat stress across scales - the most comprehensive analysis of this sort using *in situ* observations - and suggest that we should re-evaluate the current dependence on satellite-derived insights for urban design and policy making.

2. Methods

2. 1 Urban clusters and their rural backgrounds

Urban clusters over Europe are the primary regions of interest for our analysis. These clusters were generated by vectorizing contiguous 1 km x 1 km pixels classified as either low- or high-density urban in the Global Human Settlement Layer's (GHSL) settlement classification dataset (version R2016A) (Pesaresi & Freire, 2016). This aggregation of the connected urban pixels into individual urban cluster polygons is done on the Google Earth Engine cloud computing platform (Gorelick et al., 2017). Since many of these clusters are small and do not have enough citizen weather station (CWS) observations, clusters smaller than the 50th percentile of the urban cluster area distribution are removed, leaving 929 clusters (Fig. 1a).

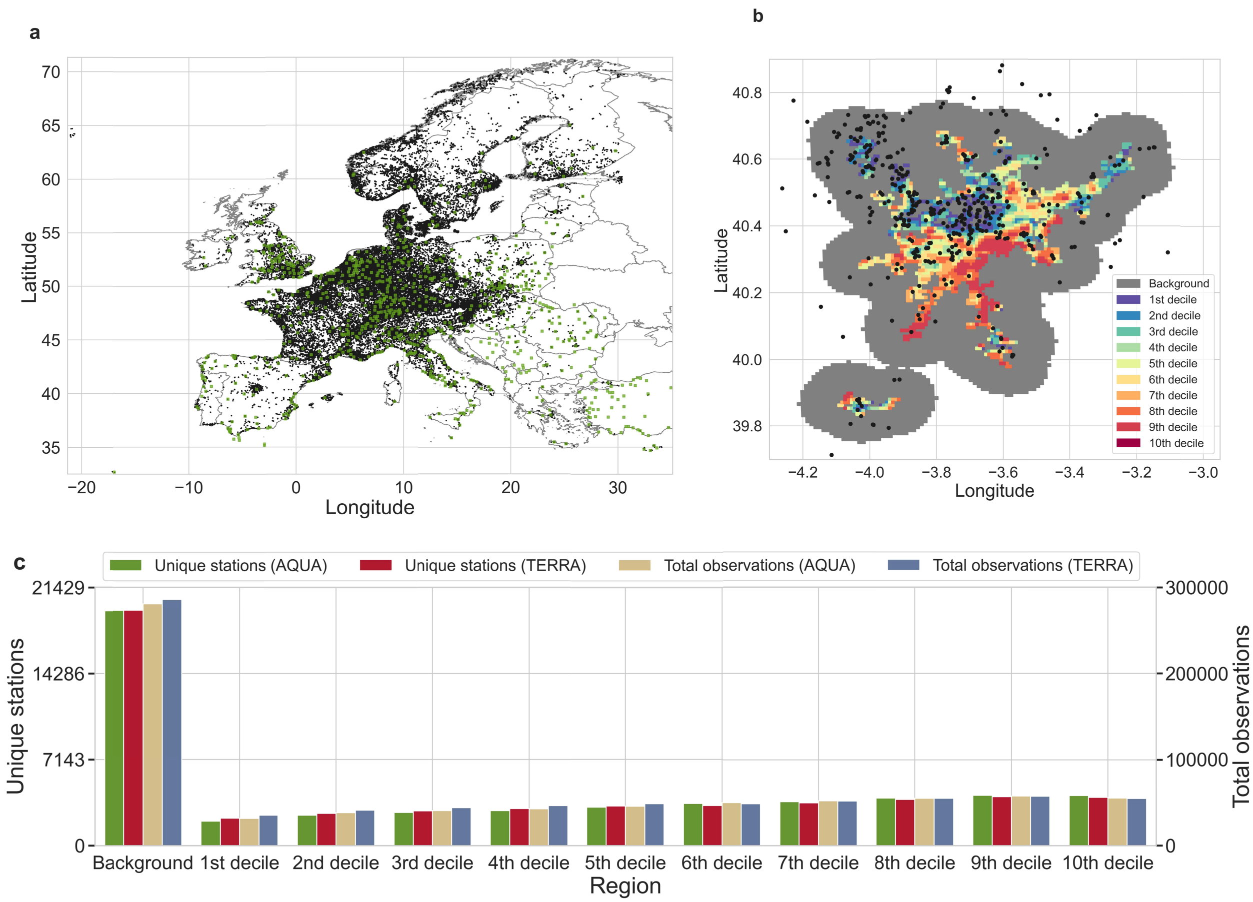

Fig. 1 Regions of interest and data summary. Sub-fig **a** shows the spatial distribution of Netatmo stations (black dots) over Europe during the heatwave of July 2019, as well as the urban clusters (in green) in the region. Sub-fig **b** shows an example of the daytime (≈1:30 pm) surface temperature (T_s) decile neighborhoods within an urban cluster (from up to 10th to 90th-100th percentile) based on daily MODIS Aqua scenes. Similar regions are created corresponding to

Terra observations (not shown). The black dots show the Netatmo stations over the cluster and the gray region represents the rural reference. Sub-fig **c** shows the total number of valid observations and unique stations for each region that correspond to the Terra and Aqua overpass times.

The rural or background reference for each cluster is a polygon buffer of 10 km width surrounding it (Fig. 1b), a definition of rural reference used in a previous global-scale study (Clinton & Gong, 2013). Since some urban clusters are closer to each other than 20 kms, a focal mode smoothing function is applied to prevent any overlap between the rural references of nearby clusters. This function designates a border between two overlapping buffers such that they are equidistant to the original urban clusters they surround. More information about the generation of the urban clusters and their rural references can be found in Venter et al. (Venter et al., 2021).

2.2 Citizen weather station data

All hourly T_a and RH observations from CWSs over Europe were downloaded for July 2019 from Netatmo (https://netatmo.com/). This includes data from 113,215 stations during this period. CWSs data have errors and biases related to less-than-ideal sensor placement, insufficient site metadata, lack of radiation shield, and instrumental errors (Meier et al., 2017). We follow a quality-control procedure developed for these sensors using the "Crowd-QC" package in R (Napoly et al., 2018). The quality-control procedure starts with removal of statistical outliers using a modified z-score approach and the hourly T_a distributions. Then, sites for which the measured T_a, when correlated against the spatial median of monthly T_a, show Pearson's correlation coefficients less than 0.9, are removed. These steps reduce the number of available stations to 95,084.

Since we wanted to get representative values for July 2019, we also removed Netatmo stations with more than 20% missing data during this period, leaving 75,293 stations. This threshold was found sufficient to capture the monthly climatological state in a previous study (Venter et al., 2021). We note that most of the quality-control procedure has been developed for T_a, not RH. However, since the Netatmo sensor module houses both T_a and RH sensors, issues related to sensor misplacement and instrumental errors would also minimize errors in measured RH. This is also confirmed through validation of the CWS measurements (see corresponding subsection below).

2.3 Calculating apparent temperature and other heat indices

Since humans primarily thermoregulate through sweating, the moisture content of the air limits our body's ability to dissipate heat, making it an important factor in addition to T_a when studying heat stress (Sherwood & Huber, 2010). There are multiple metrics of heat stress that account for moisture. In the present study, we use the heat index used by the US National Weather Service (NWS), also known as apparent temperature. This index (HI_0) is calculated in multiple steps. We start with a simple formula whose results are consistent with those from Steadman, 1979 (Steadman, 1979):

$$HI_0 = 0.5 \times [T_a + 61 + [(T-68) \times 1.2] + (0.094RH)] \tag{1}$$

where T_a is in °F and RH is in percentage. If the average of T_a and this heat index is less than 80 °F, this is the final equation used. It the average is equal to or above 80°F, the Rothfusz regression (Rothfusz, 1990) is used instead, given by:

$$\begin{aligned} \mathrm{HI}_0 = &-42.379 + 2.04901523T_\mathrm{a} + 10.14333127\mathrm{RH} - 0.22475541T_\mathrm{a}\mathrm{RH} - 6.83783 \\ &\times 10^{-3}T_\mathrm{a}^2 - 5.481717 \times 10^{-2}\mathrm{RH}^2 + 1.22874 \times 10^{-3}T_\mathrm{a}^2\mathrm{RH} + 8.5282 \\ &\times 10^{-4}T_\mathrm{a}\mathrm{RH}^2 - 1.99 \times 10^{-6}T_\mathrm{a}^2\mathrm{RH}^2 \end{aligned} \tag{2}$$

Similar to Eq. 1, the T_a is input in °F. Additional adjustments are made for low and high values of RH, consistent with the method used in operational heat warning systems by the US NWS (Rothfusz, 1990).

To check the consistency of our results, we also consider several other empirical approximations of heat stress that combine the impact of T_a and moisture, including the humidex (Masterton & Richardson, 1979) and one of each functional forms of the heat index approximation in °C reviewed in Anderson et al. (2013)

The humidex can be expressed as:

$$\mathrm{Humidex} = T_\mathrm{a} + 0.5555 \times \left(6.11 \times e^{5417.753\times\left(\frac{1}{273.16}-\frac{1}{273.15+T_\mathrm{D}}\right)} - 10\right) \tag{3}$$

where T_D is the dew-point temperature in °C and is given by:

$$T_D = \frac{243.04 \times \left\{ln\left(\frac{\mathrm{RH}}{100}\right) + \frac{17.625 \times T_a}{243.04 + T_a}\right\}}{17.625 - \left\{ln\left(\frac{\mathrm{RH}}{100}\right) + \frac{17.625 \times T_a}{243.04 + T_a}\right\}} \quad (4)$$

Finally, the other four functional forms of the heat index considered here are denoted by HI_1, HI_2, HI_3, and HI_4 and given by:

$$\mathrm{HI}_1 = T_\mathrm{a} - 1.0799e^{0.03755T_\mathrm{a}}\left(1 - e^{0.0801(T_\mathrm{D} - 14)}\right) \quad (5)$$

$$\mathrm{HI}_2 = -2.653 + 0.994T_\mathrm{a} + 0.0153{T_\mathrm{D}}^2 \quad (6)$$

$$\begin{aligned}\mathrm{HI}_3 = &-8.7847 + 1.6114T_\mathrm{a} - 0.012308T_\mathrm{a}^2 \\ &+\mathrm{RH}[2.3385 - 0.14612T_\mathrm{a} + (2.2117 \times 10^{-3})T_\mathrm{a}^2] \\ &+\mathrm{RH}^2[-0.016425 + (7.2546 \times 10^{-4})T_\mathrm{a} + (-3.582 \times 10^{-6})T_\mathrm{a}^2]\end{aligned} \quad (7)$$

$$\mathrm{HI}_4 = T_a - 0.55 \times (1 - 0.001\mathrm{RH})(T_a - 14.5) \quad (8)$$

In addition to these heat indices, we also calculate the wet-bulb temperature (T_w), a thermodynamic measure of how effectively humans can cool down via sweating (Sherwood & Huber, 2010) and a metric for heat stress often used in climate-related studies (Mishra et al., 2020; Raymond et al., 2020; L. Zhao et al., 2021), using the formulation proposed by Stull (2011).

2.4 Research-grade weather station data

To evaluate the CWS measurements, we acquired observations from the European Climate Assessment & Dataset (ECA&D) weather stations (ECA&D, 2013) for July 2019. The ECA&D dataset provides daily observations from meteorological stations throughout Europe. We extract daily T_a and RH from this network and calculate HI_0 using Eqs 1 and 2.

2.5 Reanalysis data

We also extract hourly and monthly T_a, T_D (RH is not provided by this dataset), surface pressure, and accumulated precipitation from the ECMWF (European Centre for Medium-Range Weather Forecasts) Reanalysis 5th Generation Land (ERA5-Land) dataset (Muñoz-Sabater et al., 2021). The ERA5-Land provides surface variables at high (≈9 km) resolution and is based on the tiled ECMWF Scheme for Surface Exchanges over Land incorporating land surface hydrology (H-TESSEL) and is constrained by multiple observational datasets (Muñoz-Sabater et al., 2021).

The hourly RH is computed by dividing the saturation vapor pressure (e_s) at T_D by the saturation vapor pressure at T_a, both calculated using the Clausius-Clapeyron equation (Iribarne & Godson, 1981). Thus:

$$\mathrm{RH} = 100 \times \frac{e_s(T_D)}{e_s(T_a)}) \quad (9)$$

$$e_s(T) = 6.11e^{\left[\frac{L_v}{R_v}\left(\frac{1}{273.15}-\frac{1}{T}\right)\right]} \quad (10)$$

where T is the temperature (either T_a or T_D) in Kelvin, L_v is the latent heat of vaporization of water (2.501×10^{-6} J kg^{-1}), and R_v is the specific gas constant for water vapor (461 J K^{-1} kg^{-1}).

2.6 Validating citizen weather station data

Since the ECA&D weather stations are generally not set up in cities, we start by matching each ECA&D station with rural Netatmo stations that are within a buffer of 2000 m. Some of the ECA&D stations have daily mean RH of 100% for almost the entire month, which is physically implausible. These are removed from the analysis. For each day that measured T_a and RH are available for a valid ECA&D station, we choose the corresponding Netatmo stations that include all 24 hours of observations to reliably compute the daily means. The composite means for the whole period (July 2019) from ECA&D and the Netatmo sensors are then correlated (Figs. 2a to 2c). A few of the Netatmo sensors show implausibly large differences in mean daily T_a (>10 °C) from the corresponding ECA&D measurements. To account for this in a statistically robust manner, we remove Netatmo stations whose difference in measured T_a and RH with its nearby ECA&D station is above 99 percentile or below 1 percentile of the whole distribution. These stations are not used for any of the subsequent analyses.

Overall, the CWS-measured T_a and RH show strong correlations with ECA&D observations (r^2 = 0.8 and 0.53, respectively; Figs. 2a and 2b) during this period. The root-mean-square-error (RMSE) and mean bias error (MBE) are both reasonably small (RMSE = 1.85 °C and MBE = 1.63 °C for T_a; 5.47% and -2.82% for RH). The Netatmo sensors overestimate T_a and underestimate RH, which would be expected if they often lack radiation shields (Da Cunha, 2015). However, the distribution of HI_0 is well captured by these sensors (Fig. 2c).

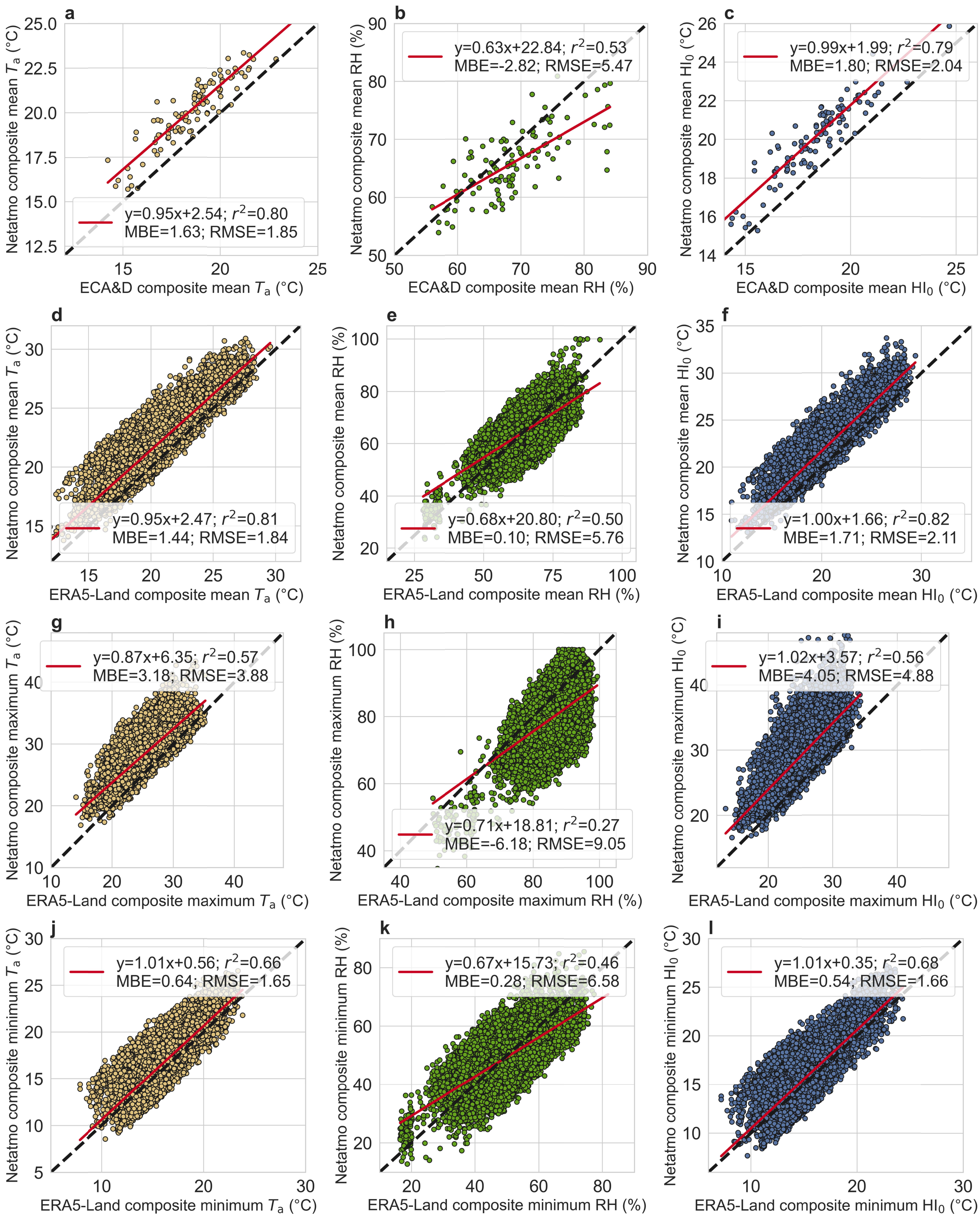

Fig. 2 Validation of citizen weather station data. Composite mean Netatmo **a** air temperature (T_a), **b** relative humidity (RH), and **c** heat index (HI_0) against corresponding European Climate

Assessment & Dataset (ECA&D) weather stations for the whole study period (July 2019). Sub-figures **d**, **e**, **f**, **g**, **h**, **i**, **j**, **k**, and **l** show composite mean (**d**, **e**, and **f**), maximum (**g**, **h**, and **i**), and minimum (**j**, **k**, and **l**) Netatmo observations against corresponding ECMWF (European Centre for Medium-Range Weather Forecasts) Reanalysis 5th Generation Land (ERA5-Land) gridded values. Each dot represents a composite value and the corresponding metrics for evaluation are shown in the legend.

The use of daily mean values for evaluation would underestimate the biases caused due to the lack of radiation shields during daytime. Although the ECA&D dataset includes maximum and minimum T_a for each station, it only includes daily mean RH, which would not allow us to calculate the maximum and minimum HI_0. Instead, we use the maximum and minimum composite values (in addition to daily means) from ERA5-Land data to compare against the corresponding rural Netatmo measurements (Figs. 2d to 2l) after removing daily differences greater than 99 percentile and less than 1 percentile of the distribution. Consistent with the comparisons with ECA&D, the Netatmo measurements overestimate T_a and HI_0 (Fig. 2d, 2f). The maximum composite T_a, which would be generally in the early afternoon (Fig. S1a), is overestimated more (MBE = 3.18 °C) than the mean composite T_a (MBE = 1.44 °C). For minimum values, generally during early morning, the biases are much smaller, with even smaller biases for HI_0 (Fig. 2l). For all cases, there is compensation between the biases due to T_a and RH, leading to slopes closer to 1 for HI_0 than for T_a.

Note that the larger spread between the ERA5-Land and Netatmo is expected since these estimates are at different scales. A Netatmo measurement represents information for a small footprint around the CWS, while the ERA5-Land estimate is for a ≈9 km grid overlaying that Netatmo site. Although there are biases between the Netatmo data and the point and gridded estimates, the distributions are captured well by the CWSs, particularly for T_a and HI_0, with slopes close to 1 (Fig. 2). Since we focus on the spatial distribution of these variables (within and between cities), not their absolute magnitudes, we are confident about our results.

2.7 Decile neighborhoods of urban skin temperature

To estimate the gradient of mean T_s within urban clusters during the study period, we first calculate the 10th to 100th percentile of T_s within each cluster using Moderate Resolution Imaging

Spectroradiometer (MODIS) observations (MYD11A1.006 and MOD11A1.006) (Wan, 2006). These percentile values are from the mean pixel-level information (by averaging available daily satellite scenes) for July 2019. Different percentile values are obtained for the four cases, namely Terra daytime overpass (≈10:30 am local time), Aqua daytime overpass (≈1:30 pm local time), Terra nighttime overpass (≈10:30 pm local time), and Aqua nighttime overpass (≈1:30 am local time). Of these, we focus mostly on the daytime values, particularly for the Aqua overpass, which is close to the time of maximum T_a and HI_0 (Fig. S1). Using these percentile values as boundary conditions, we separate each urban cluster into 10 decile neighborhoods, with each neighborhood representing a decile of T_s variation. In other words, pixels with July mean T_s values between >0th and 10th percentile of all mean T_s values in a cluster are put into the 10th percentile neighborhood (or first decile neighborhood), and so on till the 100th percentile neighborhood or 10th decile neighborhood, which includes mean T_s values between >90th and 100th percentile. The decile neighborhoods are different for Terra and Aqua as well as for days and nights. An example of these decile neighborhoods is shown for Madrid, Spain in Fig. 1b. Note that, for this particular cluster, the T_s gradient does not increase as we reach the city center. This is intended since our goal is to examine whether the decile neighborhoods, as determined by satellite observations (as has been frequently done in recent studies), is a reasonable proxy for the T_a and heat stress gradients.

After the decile neighborhoods are generated, each Netatmo station is grouped into a neighborhood for the four cases corresponding to the satellite overpass times. All these geospatial analyses are done on the Google Earth Engine platform (Gorelick et al., 2017).

2.8 Matching CWS data with satellite-derived estimates

We extract the daily T_s and exact MODIS viewing time for each ≈1 km pixel corresponding to the Netatmo stations that are either in a T_s decile neighborhood or in the rural background. The satellite viewing time is then converted from local time to coordinated universal time (UTC) based on the recommendations in the MODIS user guide (Wan, 2006) of subtracting (in hours) the quotient when dividing the longitude of the pixel (in this case, the CWS location) by 15 degrees and then adjusting by the daily hour bounds (>24 hours or <0 hours). The Netatmo observations are then matched with the daily MODIS T_s when the Netatmo observation time is within 30 minutes of the MODIS viewing time.

Similar to T_s, we also extract the Normalized Difference Vegetation Index (NDVI), a satellite-derived proxy for live green vegetation (Rouse et al., 1974), from MODIS observations. This index takes advantage of the fact that plants absorb light in the red (RED) bands and reflect near-infrared (NIR) radiation since it cannot be used photosynthesis, and is given by:

$$\mathrm{NDVI} = \frac{\mathrm{NIR-RED}}{\mathrm{NIR+RED}} \tag{11}$$

The NDVI values are derived from 16-day composites corresponding to each Netatmo station and daytime overpass (MYD13A2 and MOD13A2 for Aqua and Terra, respectively) and joined with all observations at that station. The monthly means of NDVI for July 2019 are used for the final analysis since daily variability is not as relevant for NDVI and urban surface vegetation would remain relatively unchanged within a single month. In all cases, only clear-sky pixel values are used for analysis and satellite observations for the days with missing Netatmo observations (both T_a and RH) due to quality-screening are also removed.

We also calculate monthly precipitation rate corresponding to each cluster from the monthly composite generated from the passive-microwave observations from the Global Precipitation Measurement (GPM) mission (NASA Goddard Earth Sciences Data And Information Services Center, 2019). This is done to examine how urban-rural differences in the variables of interest (see below) vary with the moisture availability of the background climate.

2.9 Urban-rural differences

Netatmo stations within the urban clusters and their corresponding satellite-derived values are used to estimate the urban T_a ($T_{a,u}$), RH ($\mathrm{RH_u}$), $\mathrm{HI_0}$ ($\mathrm{HI_{0,u}}$), T_s ($T_{s,u}$), and NDVI ($\mathrm{NDVI_u}$). The corresponding rural variables, $T_{a,r}$, $\mathrm{RH_r}$, $\mathrm{HI_{0,r}}$, $T_{s,r}$, and $\mathrm{NDVI_r}$ are from the stations in the background reference areas. Only those cases were considered for which there were at least 10 stations in both the urban clusters and their surrounding references. This leaves 557 (603) urban clusters with 40560 (42745) unique stations for Aqua (Terra) daytime overpass. The urban-rural differences are thus:

$$\Delta T_a = T_{a,u} - T_{a,r} \tag{12}$$

$$\Delta \mathrm{RH} = \mathrm{RH_u} - \mathrm{RH_r} \tag{13}$$

$$\Delta \mathrm{HI_0} = \mathrm{HI_{0,u}} - \mathrm{HI_{0,r}} \tag{14}$$

$$\Delta T_s = T_{s,\mathbf{u}} - T_{s,\mathbf{r}} \quad (15)$$

$$\Delta \mathrm{NDVI} = \mathrm{NDVI}_{\mathbf{u}} - \mathrm{NDVI}_{\mathbf{r}} \quad (16)$$

Of these, ΔT_a is equivalent to the commonly studied canopy urban heat island (CUHI) and ΔT_s is the surface urban heat island (SUHI) (Bonafoni et al., 2015; Chakraborty et al., 2017; Du et al., 2021; Venter et al., 2021). Although RH is a function of both absolute moisture content and ambient temperature, we call its urban-rural differences the urban dry island (UDI) effect since it is one of the variables used to estimate HI_0 (Eq. 1). There is currently lack of consensus on a standard metric for urban moisture content, though it is commonly accepted that urban areas are drier due to removal of vegetation and pervious surfaces (Z. Wang et al., 2021). For comparison, we also calculate the difference in absolute humidity (AH) between urban areas and their background references by combining the Netatmo observations with surface pressure estimates from ERA5-Land (Muñoz-Sabater et al., 2021). During the Aqua daytime overpass, roughly 54.3% of the urban clusters show lower AH than their background references with a mean ΔAH of -8.7×10^{-5} kg m^{-3}, confirming the presence of UDIs using both RH and AH. Similar urban-rural differences are also calculated for the Humidex and the other heat indices. The use of the MODIS pixels overlaying the Netatmo locations to calculate ΔT_s leads to reasonable apples-to-apples comparison. This might explain why our correlation coefficient between ΔT_s and ΔT_a (Fig. 7a) is slightly higher than that in a previous study (Venter et al., 2021), which compared the Netatmo-derived ΔT_a with urban cluster mean ΔT_s.

2.10 Intra-urban gradients

Although the analysis above is done for co-located pixels, the threshold for the minimum number of stations used (10) is insufficient to represent the mean climatic state of the clusters. Moreover, it is important to also analyze how well T_s, which has been extensively used as a proxy for the intra-urban variability in urban temperatures (Benz & Burney, 2021; Chakraborty et al., 2019, 2020; Hoffman et al., 2020; Hsu et al., 2021; Hulley et al., 2019), represents the within-city variability in HI_0. To address this, we estimate the intra-urban gradients in T_s, T_a, RH, and HI_0. The intra-urban gradient in station-level $T_\mathbf{s}$ is calculated by first choosing those clusters with at least 10 stations in every decile neighborhood as well as the rural background, and then averaging the daily pixel-level MODIS $T_\mathbf{s}$ in July 2019 that also had CWS measurements of T_a and RH for each region. This analysis allows us to check how well the Netatmo observations capture the overall spatial variability in T_s, as represented by the decile neighborhoods, using the corresponding T_s pixels overlaying those stations. The average value of the satellite-derived T_s for the pixels overlaying the Netatmo stations increase for increasing decile neighborhoods in all clusters (Figs. 2, S4). Similarly, the gradients corresponding to these regions for T_a, RH, and thus HI_0 are computed from the corresponding hourly Netatmo measurements. Figure 1c shows the total number of observations as well as the number of unique Netatmo stations considered when calculating these intra-urban gradients corresponding to the Terra and Aqua daytime overpass. Overall, we use 153 and 155 clusters to generate intra-urban gradients corresponding to Aqua and Terra daytime overpass.

2.11 Statistical analysis

To check whether the distributions of the chosen variables (T_s, T_a, RH, HI_0, Humidex, HI_1, HI_2, HI_3, and HI_4) are statistically different between regions (either between urban clusters and their rural backgrounds or between the rural backgrounds and the decile neighborhoods), we use the Mann –Whitney two-sample test (Wilcoxon et al., 1992). This nonparametric test allows us to check if two samples come from the same population, with lower p-values supporting the rejection of the null hypothesis that both the distributions are same. We choose a significant level of 0.01 to reject the null hypothesis, but also specify when the p-value is below 0.001 and 0.0001 in the summary tables (Tables S1, S2, S3, S4).

In addition to simple linear regressions between pairs of variables to test for their correlation and sensitivity, we also separate the control of T_a and RH on the intra-urban gradient of HI_0 within clusters by representing HI_0 as a linear combination of T_a and RH:

$$HI_0 = \alpha_1 T_a + \alpha_2 RH \qquad (17)$$

where α_1 and α_2 are the sensitivities of HI_0 to T_a and RH, respectively, as determined using multiple linear regressions for each urban cluster (Fig. 3a). Since T_a and RH have widely different range of values, we also consider a standardized form of this representation, given by:

$$HI_0 = \alpha_{1,\mathrm{std}} \frac{T_a}{T_{a,r}} + \alpha_{2,\mathrm{std}} \frac{RH}{RH_r} \qquad (18)$$

where $T_{a,r}$ and RH_r are the corresponding mean values for the rural backgrounds and the standardized sensitivities are $\alpha_{1,\mathrm{std}}$ and $\alpha_{2,\mathrm{std}}$ (Fig. 3b). A similar linear model is also used to express ΔHI_0 as a function of ΔT_a and ΔRH.

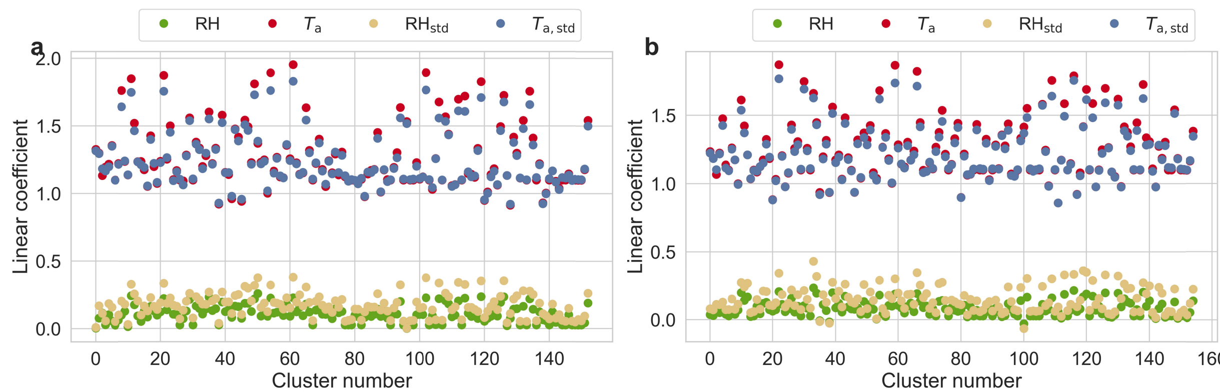

Fig. 3 Control of air temperature and relative humidity on heat stress. Values of coefficients of multi-linear regressions (of the form $HI_0 = \alpha_1 T_a + \alpha_2 RH$) for all urban clusters in Europe that have sufficient data for **a** Aqua and **b** Terra overpass times, respectively. The $_{std}$ values correspond to similar multi-linear regressions, but with standardized variables (i.e. $HI_0 = \alpha_{1,std}\frac{T_a}{T_{a,r}} + \alpha_{2,std}\frac{RH}{RH_r}$) where $_r$ variables are for the rural background.

3. Results

3.1 Urban-rural differences in temperature, humidity, and heat stress

Across 557 urban clusters in Europe (Fig. 1a), the mean ΔT_s (urban minus rural T_s) corresponding to the Aqua satellite's daytime overpass (≈1:30 pm local time) was 2.06 °C (5th percentile = -1.3 °C; 95th percentile = 5.25 °C) based on satellite observations over 40560 unique CWSs with data availability after quality screening (Fig. 4a). At ≈10:30 am local time, corresponding to the Terra satellite's daytime overpass, the mean ΔT_s over 603 clusters was slightly lower at 1.68 °C (5th percentile = -1.22 °C; 95th percentile = 4.48 °C; Fig. S2a). In contrast, the mean urban-rural difference in T_a (ΔT_a) from the CWS measurements was only 0.12 °C (5th percentile = -1.92 °C; 95th percentile = 2.19 °C) at ≈1:30 pm (Fig. 4b) and 0.05 °C (5th percentile = -2.18 °C; 95th percentile = 2.17 °C) at ≈10:30 am (Fig. S2b). The lower ΔT_a than ΔT_s during daytime is consistent with previous results from various data sources and at multiple scales (Chakraborty et al., 2017; Du et al., 2021; Ho et al., 2016; Hoffman et al., 2020; Venter et al., 2021; Zhang et al., 2014). Urban areas are also generally drier than their surroundings, with a mean urban-rural difference in RH (ΔRH) of -0.6% (5th percentile = -7.16%; 95th percentile = 6.43%) for the Aqua daytime overpass (Fig. 4c). The mean HI_0 at urban CWSs is slightly higher than that for rural CWSs (mean urban-rural difference in HI_0 (ΔHI_0) = 0.08 °C; 5th percentile = -2.28 °C; 95th percentile = 2.58 °C; Fig. 4d).

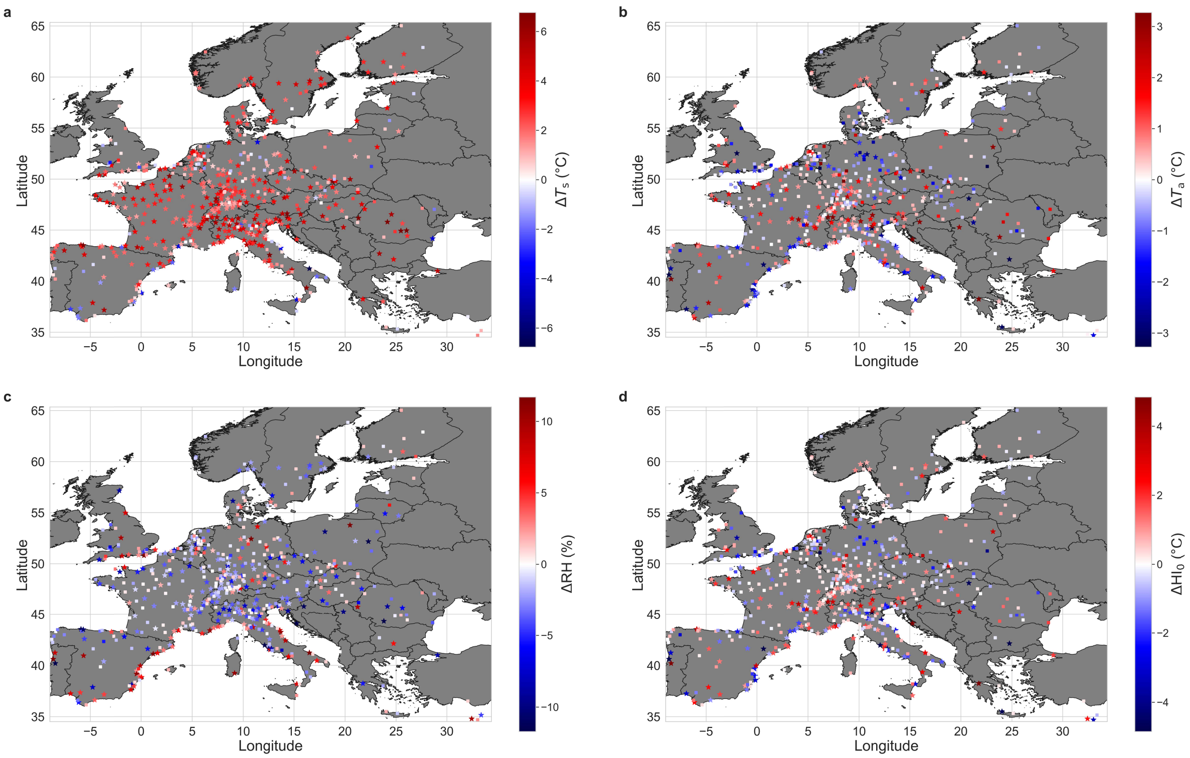

Fig. 4 Urban-rural differences for Aqua day across urban clusters. Spatial distribution of urban-rural differences in **a** radiative skin temperature (ΔT_s), **b** air temperature (ΔT_a), **c** relative humidity (ΔRH), and **d** heat index (ΔHI_0) for urban clusters in Europe at ≈1:30 pm local time. The stars represent clusters with statistically significant ($p<0.01$) differences between urban and rural values.

Evidently, due to differences in urban and rural characteristics as well as uncertainties and lack of statistical representativeness of the measurements, there are large variabilities. However, the larger scale patterns are consistent, with 87.6% (488) of the clusters showing positive ΔT_s (with 73.1% showing statistically significant differences from zero at the significance level of 0.01), which goes down to 55.1% for positive ΔT_a (37% with statistically significant differences) and 54.8% for positive ΔHI_0 (31.8% with statistically significant differences) for the Aqua daytime overpass. Similar patterns are seen corresponding to the Terra daytime overpass (Fig. S2). In both cases, urban areas are generally drier than their surroundings or ΔRH is negative (59.8% of clusters at ≈1:30 pm and 58.8% at ≈10:30 am), which would reduce HI_0, all else remaining constant. We find ΔT_a to be over eleven times more important for modulating ΔHI_0 than ΔRH (correlation coefficients of 1.37 and 0.12 for ΔT_a and ΔRH, respectively, from a multiple linear regression). Although the compensating effects of T_a and RH on HI_0 makes conceptual sense, what is surprising is that the urban-rural differences in HI_0 is so close to zero for cities during a heatwave period, with less than a third showing statistically significant differences between the urban area and its rural reference. These results weaken a common premise in many previous studies where increased urban T_s is expected to indicate adverse urban impact on overall heat vulnerability (Hsu et al., 2021; Manoli et al., 2019; Mentaschi et al., 2022; L. Zhao et al., 2017).

Consistent with previous observational and modeling estimates (Chakraborty & Lee, 2019; Manoli et al., 2019; L. Zhao et al., 2014), ΔT_s is higher for wetter climate and lower for drier areas, as seen when binned by quartiles of precipitation rate or accumulated precipitation for the same period (Figs. S3a, S3e). However, this relationship with background climate weakens for ΔT_a (Figs. S3b, S3f) and almost disappears for ΔHI_0 (Figs. S3d, S3h), evidently due to thermodynamic moisture feedback through ΔRH (Figs. S3c, S3g). As such, generalized mitigation strategies derived from information about background climate (Manoli et al., 2019) may reduce ΔT_s but would have a much smaller impact on ΔHI_0.

3.2 Spatial gradients in the urban thermal environment

Several studies (Benz & Burney, 2021; Chakraborty et al., 2019; Hsu et al., 2021; Hulley et al., 2019; Maimaitiyiming et al., 2014) have examined intra-urban variability in temperature using satellite-derived T_s. To test whether T_s is a useful proxy for urban heat stress variability within cities, we calculate the intra-urban gradients in T_s, T_a, RH, and HI_0 using those clusters (153 for Aqua and 155 for Terra) with enough (>10) CWSs in each decile neighborhood and the rural background (see Methods; Fig. 5). During the Aqua daytime overpass, the gradient of T_a along the decile neighborhoods is weaker than that for T_s, with 121 of the 153 clusters showing a positive slope, which goes down to 114 for HI_0. Higher T_s decile neighborhoods are generally drier, with RH showing a negative slope with increasing T_s in 83.6% (128) of the clusters (Fig. 6a). Overall, the relationship between T_s and T_a, although positive (mean correlation coefficient r = 0.34), shows a sensitivity (given by the slope of the linear regressions) much lower than 1 (mean slope = 0.12; Fig. 6a). This sensitivity decreases further for HI_0 (0.09) due to the compensating effects of decreasing RH and increasing T_a on HI_0 (Fig. 6b). The standardized T_a rises at roughly half the rate of the decrease in standardized RH within cities, with the linear sensitivity of HI_0 to T_a being around 7 times the sensitivity to RH (Fig. 3). Consequently, the urban HI_0 in only two of the decile neighborhoods show statistically significant differences ($p<0.01$) from the HI_0 in the rural background (Table S1). In contrast, 9, 7, and 3 of these 10 neighborhoods show statistically significant differences from the background climate for T_s, RH, and T_a, respectively. Similar results are seen for other heat indices (Tables S1, S2) and corresponding to the Terra daytime overpass (Fig. S4), with 9, 2,7, and 0 of these 10 neighborhoods showing statistically significant differences from the background climate for T_s, T_a, RH, and HI_0, respectively.

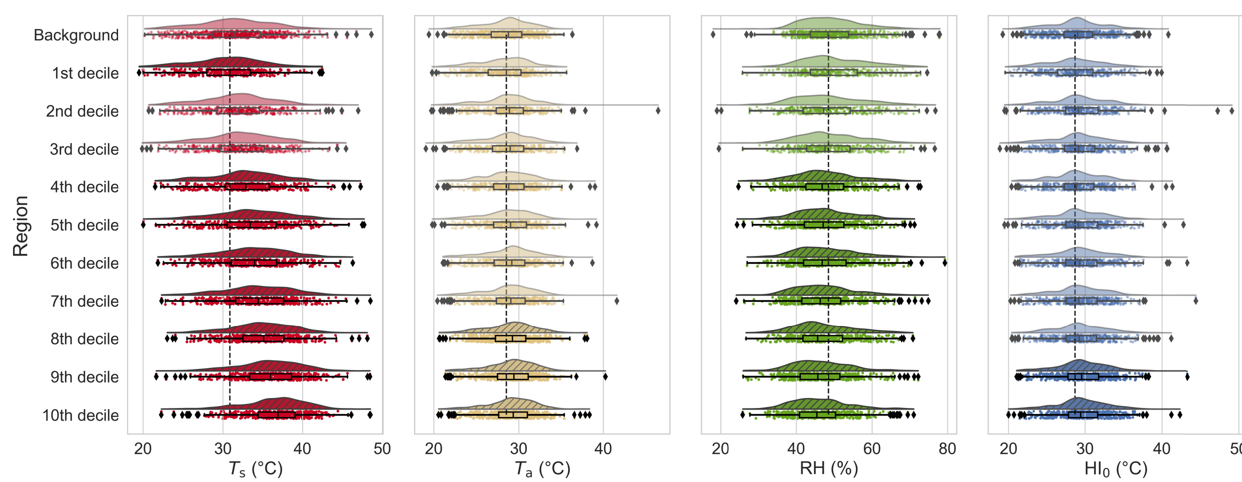

Fig. 5 Intra-urban gradients of variables. Distributions of composite mean surface temperature (T_s), air temperature (T_a), relative humidity (RH), and heat index (HI_0) in each of the T_s decile neighborhoods across the urban clusters considered. The vertical dashed lines mark the median of the distribution of the corresponding variable in the 1st T_s decile neighborhood. Decile neighborhoods that show statistically significant ($p<0.01$) differences from the background reference values are shown using hatched density plots and darker shades. All calculations are for ≈1:30 pm local time.

3.3 Role of urban vegetation

There is strong evidence of the cooling role urban vegetation has on T_s (Chakraborty et al., 2020; Chakraborty & Lee, 2019; Paschalis et al., 2021; Schwaab et al., 2021; Ziter et al., 2019), which is captured in our analysis. In 150 of the 153 clusters, the normalized difference vegetation index

(NDVI), a satellite-derived proxy for vegetation cover and vigor, is inversely correlated with T_s (Fig. 6c). However, NDVI has weaker associations with T_a (mean r = -0.81 for T_s; -0.26 for T_a), with T_a also showing a lower sensitivity to NDVI (mean slope = -3.01 °C per unit NDVI) than T_s (-26.76 °C per unit NDVI). That vegetation has a weaker control on local-scale T_a than T_s is consistent with field-level observations (Novick & Katul, 2020). The association with NDVI weakens further for HI_0, with roughly 30.7% of clusters showing a positive correlation with a weak mean sensitivity of around -2.15 °C per unit NDVI. Similar results are seen at ≈10:30 am, with 97.4% (151), 67.7% (105), and 63.2% (98) of the clusters showing a negative association with NDVI in the decile neighborhoods for T_s, T_a, and HI_0, respectively (Fig. S5c). The mean sensitivities to NDVI at ≈10:30 am range between -22.71 °C for T_s to -2.81 °C for HI_0. Similarly, the intra-urban variability in ΔHI_0 is weakly associated with ΔNDVI for both the Aqua and Terra daytime overpasses (coefficient of determination $r^2 <= 0.02$; Figs. 7h, S6h) compared to ΔT_s ($r^2 \approx 0.30$; Figs. 7e, S6e). The associations between ΔHI_0 and ΔNDVI are similarly weak at night (Fig. S7).

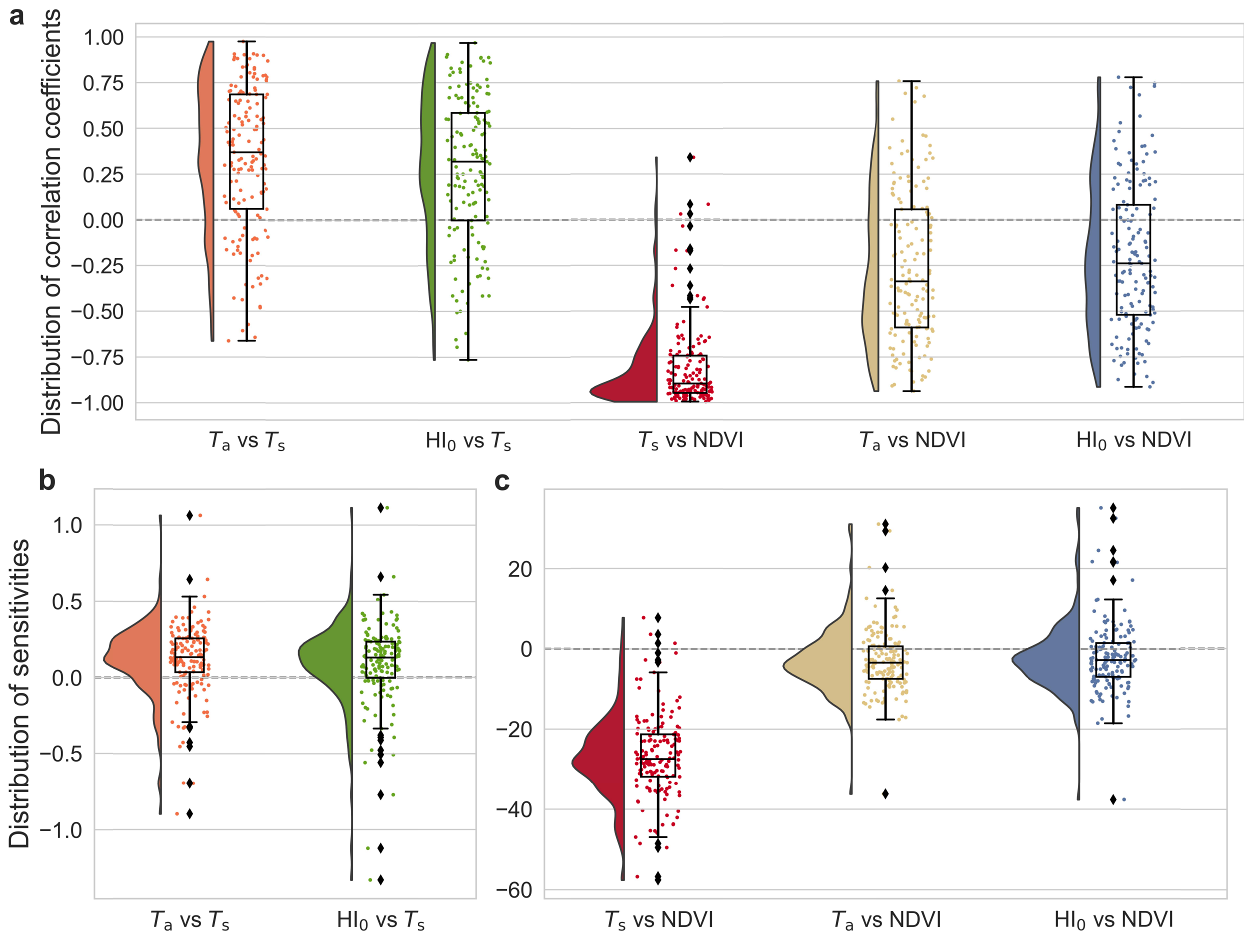

Fig. 6 Associations between variables within urban clusters. Sub-fig **a** shows the distributions of the correlation coefficient (r) of linear regressions between surface temperature (T_s) and air temperature (T_a), T_s and heat index (HI_0), Normalized Difference Vegetation Index (NDVI) and T_s, NDVI and T_a, and NDVI and HI_0, respectively, for urban clusters in Europe. Each data point is from a linear regression between pairs of variables for a cluster. The linear regressions have a sample size of ten (one for each T_s decile neighborhood). Sub-fig **b** and **c** show the distributions of the slope of those linear regressions, or the sensitivity of one variable to unit changes in the other. The unit of sensitivity in Sub-fig **c** is °C per unit NDVI. All calculations are for ≈1:30 pm local time.

4. Discussion

4.1 Deficiencies in radiative skin temperature for studying urban areas

Satellite-derived T_s is widely used for urban research (Benz & Burney, 2021; Chakraborty & Lee, 2019; Clinton & Gong, 2013; Li et al., 2019; Manoli et al., 2019; Paschalis et al., 2021; L. Zhao et al., 2014). For observational studies, this is due to the availability of global and spatially continuous satellite measurements, which enable, among other things, analyses of intra-urban and inter-urban variability; difficult using ground-based measurements. Satellite-derived T_s is also used to develop and evaluate models (Li et al., 2019; Manoli et al., 2019; L. Zhao et al., 2014). Conceptual models of T_s are easier to formulate than those for T_a or HI_0, due to strong coupling between T_s and the surface energy budget. Although T_s and T_a are not strongly correlated over urban areas, especially relevant for public health (Ho et al., 2016; Stone Jr et al., 2019), studies have assumed, either implicitly or explicitly, that ΔT_s can still be useful for making decisions about urban heat mitigation (Benz & Burney, 2021; Chakraborty et al., 2020; Hsu et al., 2021; Hulley et al., 2019; Manoli et al., 2019; L. Zhao et al., 2014). We find that for cities in Europe during a heatwave period, the correlations between urban-scale ΔT_s and ΔT_a are fairly weak, particularly during daytime (r^2 = 0.10 for Aqua; 0.09 for Terra; Figs. 4a, S6a), with only 21% of the variability in ΔT_s (slope = 0.21) among cities expected for ΔT_a.

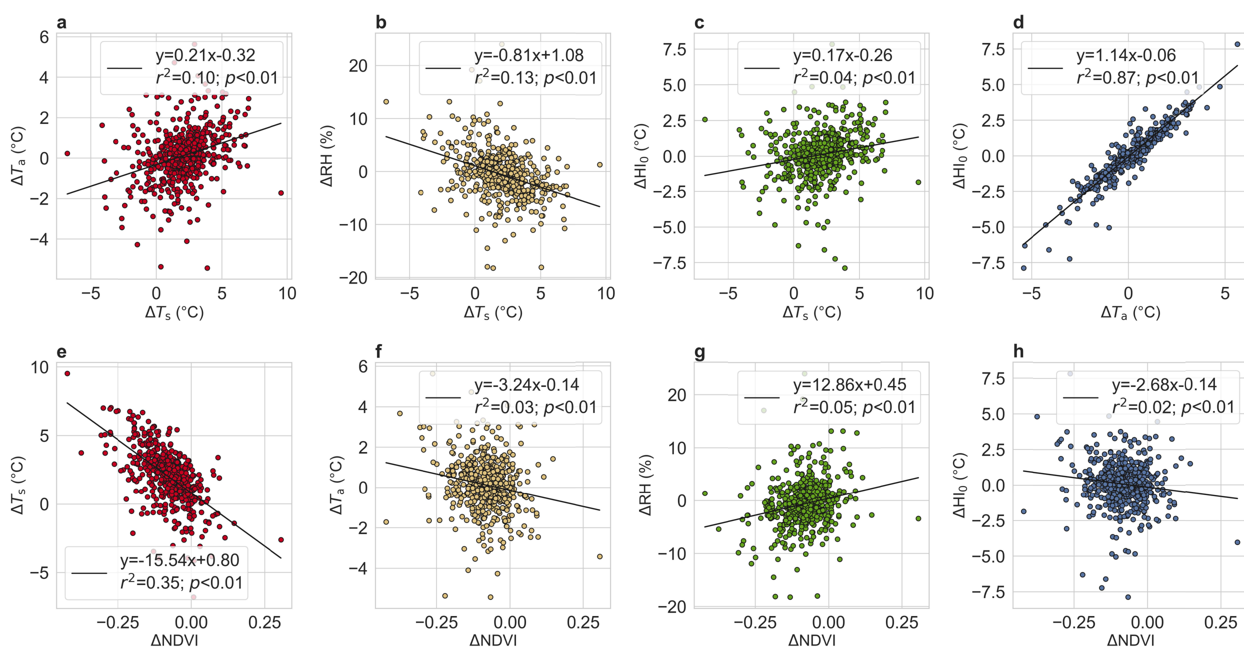

Fig. 7 Associations between variables across urban clusters. Associations between urban-rural differences in **a** radiative skin temperature (ΔT_s) and air temperature (ΔT_a), **b** ΔT_s and relative humidity (ΔRH), **c** ΔT_s and heat index (ΔHI_0), **d** ΔT_a and ΔHI_0, **e** Normalized Difference Vegetation Index (ΔNDVI) and ΔT_s, **f** ΔNDVI and ΔT_a, **g** ΔNDVI and ΔRH, and **h** ΔNDVI and ΔHI_0 across urban clusters in Europe. Each dot represents one cluster, and the lines and equations of best fit are shown. All calculations are for ≈1:30 pm local time.

Furthermore, our analysis shows that the inter-urban variability in ΔHI_0 is weaker still when correlated with that of satellite-derived ΔT_s ($r^2 = 0.04$; Figs. 7c, S6c), making T_s a poor proxy for the urban impact on heat vulnerability. As such, any insights gained using T_s, whether using observations or models, may not be strongly relevant for mitigating urbanization-induced heat stress. Note that we examine urban-rural differences to isolate the urban influence on these variables, rather than absolute heat stress, which would regulate total heat-related hazard in cities (Martilli et al., 2020). This is done to account for differences in absolute heat stress in cities due to background climate.

Coarse to medium-resolution T_s from satellites have been used for hotspot analysis within cities (Hulley et al., 2019; Maimaitiyiming et al., 2014). Several studies have taken advantage of the spatial continuity of satellite observations to map intra-urban variability of T_s across cities, with implications for environmental disparities (Benz & Burney, 2021; Chakraborty et al., 2019; Hsu et al., 2021). We find that for the cities considered here, T_s is a poor proxy for the intra-urban variability in HI_0 or other heat indices (including Humidex, used in heat warning systems). Even the 95th and 98th percentiles of hourly HI_0 ($HI_{0,95}$ and $HI_{0,98}$, respectively) do not show statistically significant differences from the background in most of the decile neighborhoods (Fig. S8 and Table S3). Future multi-city studies should focus on covariance of heat stress with socioeconomic variables to re-evaluate the magnitude of these environmental disparities, if any.

This is not to say that examining T_s over cities is pointless. Nighttime ΔHI_0 (≈1:30 am local time) is generally positive (Fig. S9), and moderately correlated with ΔT_s ($r^2 = 0.21$; $p < 0.01$) across (Fig. S7c) and within cities (Table S4), which might explain why previous studies have shown associations between nighttime T_s and heat-related mortality (Laaidi et al., 2012; Murage et al., 2017). Moreover, high T_s does increase radiant heat exposure and is the lower boundary for the atmospheric column, which consequently modulates the surface energy budget and local weather (Arnfield, 2003). Ultimately, more accurate estimates of heat stress within cities requires more ground-level observations, not just of standard meteorological variables, but also exposure to radiation and wind speed, which are not available from these CWSs. Moreover, CWS sensors are not research-grade and frequently influenced by less-than-ideal placement, insufficient site metadata, and usually lack radiation shields (Venter et al., 2021), though that last issue has minimal impact since we primarily deal with distributions, not absolute values (Fig. 2).

Urban climate research has generally encouraged urban tree planting due to their local evaporative cooling potential (Chakraborty & Lee, 2019; Li et al., 2019; Paschalis et al., 2021; Schwaab et al., 2021; Wong et al., 2021; Ziter et al., 2019). However, reductions in T_s through evaporation, which is the primary focus of these studies, do not imply equivalent reductions in T_a (Novick & Katul, 2020). This is further complicated when we consider HI_0 due to the local-scale increase in RH due to vegetation (Krayenhoff et al., 2021; Meili et al., 2020). We find that the efficiency of reducing HI_0 within cities using urban vegetation is weakened (-2.15 °C for a hypothetical unit change in NDVI, spanning half the physically possible range), as seen from the linear correlations, due to the competing effects of reduced T_a and enhanced RH. Moreover, the urban-rural differences in vegetation are not associated with the urban-rural differences in HI_0 across cities due to these same competing effects (Figs. 7f, 7g, S6f, S6g). However, note that shading effect of trees is also important and reduces the radiant heat exposure on pedestrians at the micro scale, although urban form can also serve this purpose (Middel et al., 2021; Q. Zhao et al., 2018). Moreover, there are several co-benefits of urban vegetation, from increased carbon sequestration to reduced air pollution to multiple beneficial health outcomes, beyond any reduction in local T_s (Fargione et al., 2018; Fong et al., 2018; Remme et al., 2021). Overall, mitigation strategies that rely on urban vegetation should carefully consider the realistic efficiency of street trees to improve thermal comfort at multiple scales (versus competing strategies) in addition to those other factors for cost-benefit analyses. As an aside, when the reduction in satellite-derived T_s due to surface vegetation is usually examined (Paschalis et al., 2021; Schwaab et al., 2021; Wong et al., 2021), what is compared is the association of T_s of the top of the canopy (what the satellite sees) with some measure of vegetation. Since this is not physically equivalent to what a pedestrian would feel either underneath the tree canopy or near it, we need to be cautious about quantitative estimates of the cooling potential of urban vegetation derived from satellite measurements of T_s. Similarly, models used to examine urban heat stress or urban heat mitigation must incorporate accurate urban vegetation to represent realistic cities, which is currently missing, simplistic, or still under development (Krayenhoff et al., 2020, 2021; Meili et al., 2020; L. Zhao et al., 2017, 2021).

4.2 Relative importance of humidity for heat stress

The role of humidity in human physiological response to heat is well-recognized in the epidemiological literature (Anderson et al., 2013). How important humidity is relative to T_a for heat stress is however still an open question (Anderson et al., 2013; Sherwood, 2018). For Europe, we find T_a to be around seven times more important than RH for capturing both the inter-urban and intra-urban variability in HI_0 (Fig. 3). However, HI_0 is known to have a low sensitivity to RH than many other heat indices (Sherwood, 2018). Moreover, most parts of Europe, even at their warmest, would have a further lower sensitivity of heat stress to RH due to the HI_0 formulation (Eqs 1, 2; Fig. 8a). This is particularly apparent at night, when T_a and HI_0 are found to be strongly coupled (Fig. S7d) since it uses the simple linear equation (Eq. 1) with much higher importance given to T_a. Since the impact of RH on HI_0 increases non-linearly with increasing T_a (Fig. 8a), in warmer and more humid regions, such as in the tropics, decreasing RH due to urbanization could have more noticeable effect on moderating urbanization-induced heat stress (Mishra et al., 2020). As an aside, the similar magnitudes of changes in T_a and HI_0, say when correlated with NDVI (Figs. 6c, 7f, 7h), can be misleading without contextualizing that unit changes in HI_0 are not physiologically equivalent to a unit change T_a. For instance, changing T_a from 5 to 35 °C leads to changes in HI_0 from 5 °C to over 70 °C (Fig. 8a). Ideally, these variables should be compared in the context of public health, though heat-related health-outcome data are generally not available at such scales.

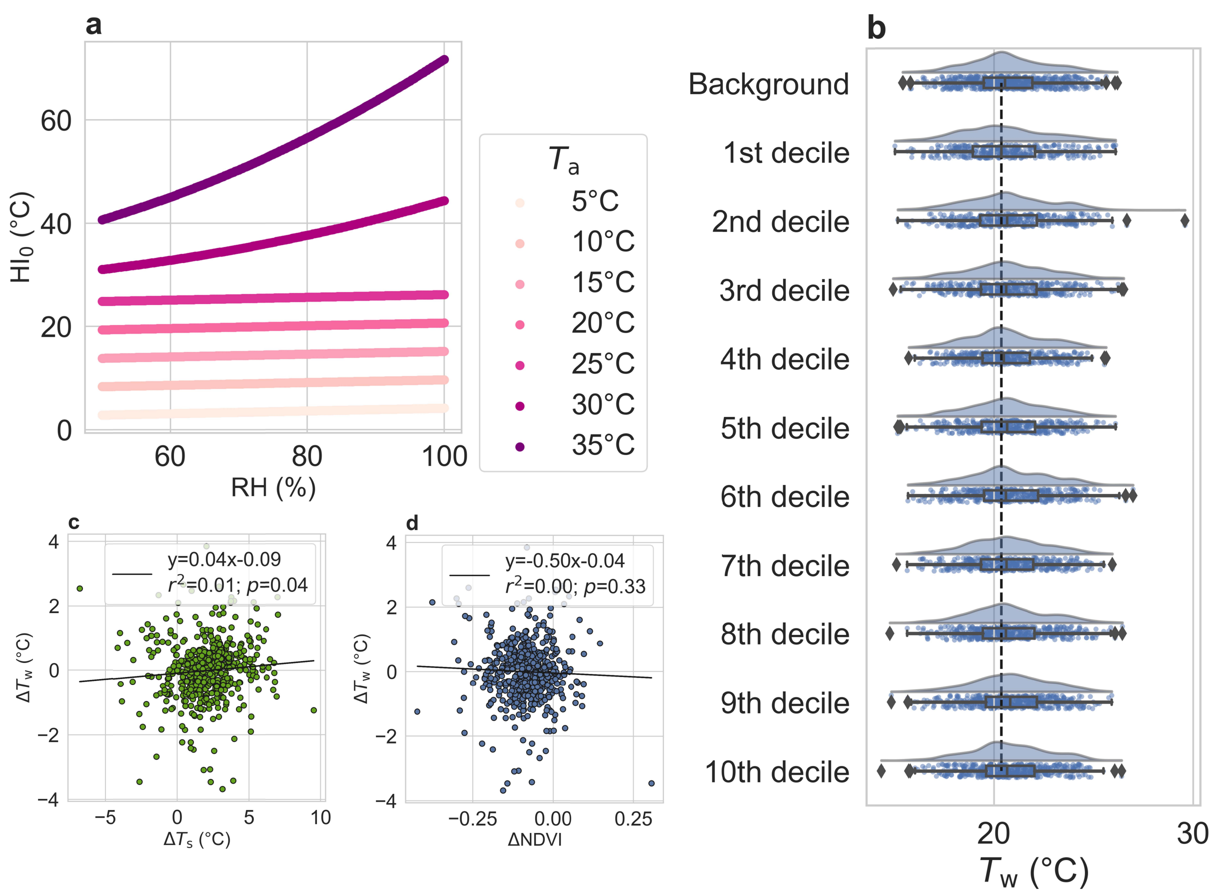

Fig. 8 Humidity and metrics of heat stress. Sub-figure **a** shows the dependence of the heat index (HI_0) used by the US National Weather Service on relative humidity (RH) for different values of air temperature (T_a). Sub-figure **b** shows distributions of composite mean surface wet-bulb temperature (T_w) in each of the T_s decile neighborhoods across the urban clusters considered (similar to Fig. 5). Sub-figure **c** and **d** show associations between urban-rural differences in radiative skin temperature (ΔT_s) and T_w (ΔT_w), and Normalized Difference Vegetation Index (ΔNDVI) and ΔT_w, respectively across urban clusters in Europe. Each dot represents one cluster and the lines and equations of best fit are shown. All calculations in sub-figures **b**, **c**, and **d** are for ≈1:30 pm local time.

Several recent climate-related studies have also used T_w as a heat stress metric (Mishra et al., 2020; Raymond et al., 2020; L. Zhao et al., 2021). In contrast to the empirical measures of heat stress, T_w has a clear thermodynamic basis, with values above 35 °C inducing hyperthermia in humans and other mammals, and even lower values of T_w having mortality and morbidity impacts (Raymond et al., 2020; Sherwood & Huber, 2010). T_w is more strongly controlled by humidity than HI_0, since it is essentially a measure of the moisture content of an air parcel. This higher sensitivity of T_w to RH can be illustrated by calculating urban-rural differences in T_w (ΔT_w). ΔT_w is slightly negative (-0.002 °C) and shows even weaker (and statistically insignificant) correlations with ΔT_s and ΔNDVI (Figs. 8c, 8d). Moreover, none of the decile regions show statistically significant differences in T_w from the background (Fig 8b). As such, although the moderating effect of decreasing RH on heat stress is both conceptually and observationally apparent, in the absence of health outcome data, the magnitude of this effect would depend on the measure of heat stress used. For use of T_w as a heat index, it should be kept in mind that only higher absolute values (above 31 °C) are valid for describing human physiological response under specific conditions (completely wet and unclothed; Sherwood, 2018).

4.3 Implications

The results of the present study do not necessarily imply that urban areas have no additional heat stress compared to their surroundings or that we should not target cities for heat mitigation. Urban areas tend to have positive nighttime ΔT_a and ΔHI_0, which contributes to mortality and morbidity during heatwaves (Laaidi et al., 2012; Murage et al., 2017). Even during daytime, we find large variabilities in ΔHI_0, and the positive ΔHI_0 would disproportionately impact public health given the high population densities in cities. Moreover, a source of uncertainty with CWS data is that they have sampling biases, with most sensors set up in residential areas, not in commercial districts where it is usually hotter (Hulley et al., 2019). Thus, we may be systematically avoiding non-residential areas when using CWS data, where pedestrians may still be exposed to higher-than-expected heat stress.

The caveats above do not undermine the observation that within cities, urbanization-induced lower RH partly compensates for the higher T_a when it comes to heat stress, and the spatial variability in this heat stress is poorly captured by satellite observations for the corresponding overlaying pixels. Although cities in other parts of the world may show differences in the strength, or lack thereof, of associations between these variables, on a conceptual level, we speculate that we will get qualitatively similar results, with T_s showing stronger variability than T_a and heat stress across scales. However, more observations are necessary to confirm this hypothesis. In summary, we find compelling observational evidence that relying on T_s to generate large-scale insights on the magnitude of urban heat stress and recommendations for urban heat mitigation may be inappropriate. On a positive note, this mediating effect of the urbanization-induced heating and drying suggest that less effort may be needed to reduce urban thermal discomfort compared to their surroundings, leading to relatively higher benefits of urban-scale mitigation strategies that focus on heat stress. It is often said that “You can't manage what you can't measure.” Our present study suggests that we may be measuring the wrong variable for quantifying and mitigating the heat-related public health consequences of urbanization. In spite of the logistic and methodological simplicity of satellite-derived T_s, we need more *in situ* observations of T_a, RH, wind speed, radiant heat, etc. to more accurately characterize the urban thermal environment and quantify the efficiency of heat stress mitigation strategies as we prepare for a warmer, wetter, and more urban future (Chen et al., 2020; W. Wang et al., 2021).

Acknowledgments

PNNL is operated for the Department of Energy by Battelle Memorial Institute under contract DE-AC05-76RL01830. The authors also thank the Yale Center for Earth Observation for providing computational resources.

T.C. designed the study, processed the satellite scenes, analyzed the data, and wrote the first draft of the manuscript. Z.S.V. extracted and processed the citizen weather station data and generated the urban-rural regions of interest. Z.S.V., X.L., and Y.Q. provided inputs on methodology and writing.

Open Research

All data will be made available through a publicly accessible repository (GitHub) on acceptance of the manuscript.

References

Anderson, G. B., Bell, M. L., & Peng, R. D. (2013). Methods to Calculate the Heat Index as an Exposure Metric in Environmental Health Research. *Environmental Health Perspectives*, *121*(10), 1111–1119. https://doi.org/10.1289/ehp.1206273

Arnfield, A. J. (2003). Two decades of urban climate research: A review of turbulence, exchanges of energy and water, and the urban heat island. *International Journal of Climatology*, *23*(1), 1–26.

Benz, S. A., & Burney, J. A. (2021). Widespread Race and Class Disparities in Surface Urban Heat Extremes Across the United States. *Earth's Future*, *9*(7). https://doi.org/10.1029/2021EF002016

Bonafoni, S., Anniballe, R., & Pichierri, M. (2015). Comparison between surface and canopy layer urban heat island using MODIS data. *2015 Joint Urban Remote Sensing Event (JURSE)*, 1–4.

Chakraborty, T., Hsu, A., Manya, D., & Sheriff, G. (2019). Disproportionately higher exposure to urban heat in lower-income neighborhoods: A multi-city perspective. *Environmental Research Letters*, *14*(10), 105003. https://doi.org/10.1088/1748-9326/ab3b99

Chakraborty, T., Hsu, A., Manya, D., & Sheriff, G. (2020). A spatially explicit surface urban heat island database for the United States: Characterization, uncertainties, and possible applications. *ISPRS Journal of Photogrammetry and Remote Sensing*, *168*, 74–88. https://doi.org/10.1016/j.isprsjprs.2020.07.021

Chakraborty, T., & Lee, X. (2019). A simplified urban-extent algorithm to characterize surface urban heat islands on a global scale and examine vegetation control on their spatiotemporal variability. *International Journal of Applied Earth Observation and Geoinformation*, *74*, 269–280. https://doi.org/10.1016/j.jag.2018.09.015

Chakraborty, T., Sarangi, C., & Tripathi, S. N. (2017). Understanding Diurnality and Inter-Seasonality of a Sub-tropical Urban Heat Island. *Boundary-Layer Meteorology*, *163*(2), 287–309. https://doi.org/10.1007/s10546-016-0223-0

Chen, G., Li, X., Liu, X., Chen, Y., Liang, X., Leng, J., Xu, X., Liao, W., Qiu, Y., Wu, Q., & Huang, K. (2020). Global projections of future urban land expansion under shared socioeconomic pathways. *Nature Communications*, *11*(1), 537. https://doi.org/10.1038/s41467-020-14386-x

Clinton, N., & Gong, P. (2013). MODIS detected surface urban heat islands and sinks: Global locations and controls. *Remote Sensing of Environment*, *134*, 294–304. https://doi.org/10.1016/j.rse.2013.03.008

Da Cunha, A. R. (2015). Evaluation of measurement errors of temperature and relative humidity from HOBO data logger under different conditions of exposure to solar radiation. *Environmental Monitoring and Assessment*, *187*(5), 1–11.

Du, H., Zhan, W., Liu, Z., Li, J., Li, L., Lai, J., Miao, S., Huang, F., Wang, C., & Wang, C. (2021). Simultaneous investigation of surface and canopy urban heat islands over global cities. *ISPRS Journal of Photogrammetry and Remote Sensing*, *181*, 67–83.

ECA&D. (2013). *European Climate Assessment & Dataset (ECA&D)'Algorithm Theoretical Basis Document (ATBD), Version 10.7.* Royal Netherlands Meteorological Institute KNMI.

Fargione, J. E., Bassett, S., Boucher, T., Bridgham, S. D., Conant, R. T., Cook-Patton, S. C., Ellis, P. W., Falcucci, A., Fourqurean, J. W., Gopalakrishna, T., & others. (2018). Natural climate solutions for the United States. *Science Advances*, *4*(11), eaat1869.

Fong, K. C., Hart, J. E., & James, P. (2018). A Review of Epidemiologic Studies on Greenness and Health: Updated Literature Through 2017. *Current Environmental Health Reports*, *5*(1), 77–87. https://doi.org/10.1007/s40572-018-0179-y

Gorelick, N., Hancher, M., Dixon, M., Ilyushchenko, S., Thau, D., & Moore, R. (2017). Google Earth Engine: Planetary-scale geospatial analysis for everyone. *Remote Sensing of Environment*, *202*, 18–27. https://doi.org/10.1016/j.rse.2017.06.031

Heaviside, C., Macintyre, H., & Vardoulakis, S. (2017). The Urban Heat Island: Implications for Health in a Changing Environment. *Current Environmental Health Reports*, *4*(3), 296–305. https://doi.org/10.1007/s40572-017-0150-3

Heilig, G. K. (2014). World urbanization prospects the 2014 revision. *United Nations, Department of Economic and Social Affairs (DESA), Population Division, Population Estimates and Projections Section, New York.*

Ho, H. C., Knudby, A., Xu, Y., Hodul, M., & Aminipouri, M. (2016). A comparison of urban heat islands mapped using skin temperature, air temperature, and apparent temperature (Humidex), for the greater Vancouver area. *Science of The Total Environment*, *544*, 929–938. https://doi.org/10.1016/j.scitotenv.2015.12.021

Hoffman, J. S., Shandas, V., & Pendleton, N. (2020). The Effects of Historical Housing Policies on Resident Exposure to Intra-Urban Heat: A Study of 108 US Urban Areas. *Climate*, *8*(1), 12. https://doi.org/10.3390/cli8010012

Howard, L. (1833). *The climate of London: Deduced from meteorological observations made in the metropolis and at various places around it* (Vol. 2). Harvey and Darton, J. and A. Arch, Longman, Hatchard, S. Highley [and] R. Hunter.

Hsu, A., Sheriff, G., Chakraborty, T., & Manya, D. (2021). Disproportionate exposure to urban heat island intensity across major US cities. *Nature Communications*, *12*(1), 2721. https://doi.org/10.1038/s41467-021-22799-5

Huang, K., Lee, X., Stone Jr, B., Knievel, J., Bell, M. L., & Seto, K. C. (2021). Persistent increases in nighttime heat stress from urban expansion despite heat island mitigation. *Journal of Geophysical Research: Atmospheres*, *126*(4), e2020JD033831.

Hulley, G., Shivers, S., Wetherley, E., & Cudd, R. (2019). New ECOSTRESS and MODIS Land Surface Temperature Data Reveal Fine-Scale Heat Vulnerability in Cities: A Case Study for Los Angeles County, California. *Remote Sensing*, *11*(18), 2136. https://doi.org/10.3390/rs11182136

Iribarne, J. V., & Godson, W. L. (1981). *Atmospheric thermodynamics* (Vol. 6). Springer Science & Business Media.

Jin, M., & Dickinson, R. E. (2010). Land surface skin temperature climatology: Benefitting from the strengths of satellite observations. *Environ Res Lett*, *5*(4), 044004.

Keith, L., Meerow, S., & Wagner, T. (2019). Planning for extreme heat: A review. *Journal of Extreme Events*, *6*(03n04), 2050003.

Krayenhoff, E. S., Broadbent, A. M., Zhao, L., Georgescu, M., Middel, A., Voogt, J. A., Martilli, A., Sailor, D. J., & Erell, E. (2021). Cooling hot cities: A systematic and critical review of the numerical modelling literature. *Environmental Research Letters*, *16*(5), 053007. https://doi.org/10.1088/1748-9326/abdcf1

Krayenhoff, E. S., Jiang, T., Christen, A., Martilli, A., Oke, T. R., Bailey, B. N., Nazarian, N., Voogt, J. A., Giometto, M. G., & Stastny, A. (2020). A multi-layer urban canopy meteorological model with trees (BEP-Tree): Street tree impacts on pedestrian-level climate. *Urban Climate*, *32*, 100590.

Laaidi, K., Zeghnoun, A., Dousset, B., Bretin, P., Vandentorren, S., Giraudet, E., & Beaudeau, P. (2012). The Impact of Heat Islands on Mortality in Paris during the August 2003 Heat Wave. *Environmental Health Perspectives*, *120*(2), 254–259. https://doi.org/10.1289/ehp.1103532

Li, D., Liao, W., Rigden, A. J., Liu, X., Wang, D., Malyshev, S., & Shevliakova, E. (2019). Urban heat island: Aerodynamics or imperviousness? *Science Advances*, *5*(4), eaau4299.

Lokoshchenko, M. A. (2017). Urban Heat Island and Urban Dry Island in Moscow and Their Centennial Changes. *Journal of Applied Meteorology and Climatology*, *56*(10), 2729–2745. https://doi.org/10.1175/JAMC-D-16-0383.1

Maia-Silva, D., Kumar, R., & Nateghi, R. (2020). The critical role of humidity in modeling summer electricity demand across the United States. *Nature Communications*, *11*(1), 1686. https://doi.org/10.1038/s41467-020-15393-8

Maimaitiyiming, M., Ghulam, A., Tiyip, T., Pla, F., Latorre-Carmona, P., Halik, Ü., Sawut, M., & Caetano, M. (2014). Effects of green space spatial pattern on land surface temperature: Implications for sustainable urban planning and climate change adaptation. *ISPRS Journal of Photogrammetry and Remote Sensing*, *89*, 59–66. https://doi.org/10.1016/j.isprsjprs.2013.12.010

Manoli, G., Fatichi, S., Schläpfer, M., Yu, K., Crowther, T. W., Meili, N., Burlando, P., Katul, G. G., & Bou-Zeid, E. (2019). Magnitude of urban heat islands largely explained by climate and population. *Nature*, *573*(7772), 55–60. https://doi.org/10.1038/s41586-019-1512-9

Martilli, A., Krayenhoff, E. S., & Nazarian, N. (2020). Is the Urban Heat Island intensity relevant for heat mitigation studies? *Urban Climate*, *31*, 100541. https://doi.org/10.1016/j.uclim.2019.100541

Masterton, J. M., & Richardson, F. A. (1979). *Humidex: A method of quantifying human discomfort due to excessive heat and humidity*. Environment Canada, Atmospheric Environment.

Meier, F., Fenner, D., Grassmann, T., Otto, M., & Scherer, D. (2017). Crowdsourcing air temperature from citizen weather stations for urban climate research. *Urban Climate*, *19*, 170–191. https://doi.org/10.1016/j.uclim.2017.01.006

Meili, N., Manoli, G., Burlando, P., Bou-Zeid, E., Chow, W. T. L., Coutts, A. M., Daly, E., Nice, K. A., Roth, M., Tapper, N. J., Velasco, E., Vivoni, E. R., & Fatichi, S. (2020). An urban ecohydrological model to quantify the effect of vegetation on urban climate and hydrology (UT&C v1.0). *Geoscientific Model Development*, *13*(1), 335–362. https://doi.org/10.5194/gmd-13-335-2020

Mentaschi, L., Duveiller, G., Zulian, G., Corbane, C., Pesaresi, M., Maes, J., Stocchino, A., & Feyen, L. (2022). Global long-term mapping of surface temperature shows intensified intra-city urban heat island extremes. *Global Environmental Change*, *72*, 102441.

Middel, A., Alkhaled, S., Schneider, F. A., Hagen, B., & Coseo, P. (2021). 50 Grades of Shade. *Bulletin of the American Meteorological Society*, 1–35. https://doi.org/10.1175/BAMS-D-20-0193.1

Mishra, V., Ambika, A. K., Asoka, A., Aadhar, S., Buzan, J., Kumar, R., & Huber, M. (2020). Moist heat stress extremes in India enhanced by irrigation. *Nature Geoscience*, *13*(11), 722–728. https://doi.org/10.1038/s41561-020-00650-8

Muller, C. L., Chapman, L., Grimmond, C. S. B., Young, D. T., & Cai, X. (2013). Sensors and the city: A review of urban meteorological networks: SENSORS AND THE CITY. *International Journal of Climatology*, *33*(7), 1585–1600. https://doi.org/10.1002/joc.3678

Muñoz-Sabater, J., Dutra, E., Agustí-Panareda, A., Albergel, C., Arduini, G., Balsamo, G., Boussetta, S., Choulga, M., Harrigan, S., Hersbach, H., Martens, B., Miralles, D. G., Piles, M., Rodríguez-Fernández, N. J., Zsoter, E., Buontempo, C., & Thépaut, J.-N. (2021). *ERA5-Land: A state-of-the-art global reanalysis dataset for land applications* [Preprint]. Data, Algorithms, and Models. https://doi.org/10.5194/essd-2021-82

Murage, P., Hajat, S., & Kovats, R. S. (2017). Effect of night-time temperatures on cause and age-specific mortality in London: *Environmental Epidemiology*, 1. https://doi.org/10.1097/EE9.0000000000000005

Napoly, A., Grassmann, T., Meier, F., & Fenner, D. (2018). Development and Application of a Statistically-Based Quality Control for Crowdsourced Air Temperature Data. *Frontiers in Earth Science*, *6*, 118. https://doi.org/10.3389/feart.2018.00118

NASA Goddard Earth Sciences Data And Information Services Center. (2019). *GPM IMERG Final Precipitation L3 1 day 0.1 degree x 0.1 degree V06* [Data set]. NASA Goddard Earth Sciences Data and Information Services Center. https://doi.org/10.5067/GPM/IMERGDF/DAY/06

Novick, K. A., & Katul, G. G. (2020). The Duality of Reforestation Impacts on Surface and Air Temperature. *Journal of Geophysical Research: Biogeosciences*, *125*.

Oleson, K. W., Monaghan, A., Wilhelmi, O., Barlage, M., Brunsell, N., Feddema, J., Hu, L., & Steinhoff, D. F. (2015). Interactions between urbanization, heat stress, and climate change. *Climatic Change*, *129*(3), 525–541.

Paschalis, A., Chakraborty, T., Fatichi, S., Meili, N., & Manoli, G. (2021). Urban Forests as Main Regulator of the Evaporative Cooling Effect in Cities. *AGU Advances*, *2*(2). https://doi.org/10.1029/2020AV000303

Perkins-Kirkpatrick, S. E., & Lewis, S. C. (2020). Increasing trends in regional heatwaves. *Nature Communications*, *11*(1), 3357. https://doi.org/10.1038/s41467-020-16970-7

Pesaresi, M., & Freire, S. (2016). GHS Settlement grid following the REGIO model 2014 in application to GHSL Landsat and CIESIN GPW v4-multitemporal (1975-1990-2000-2015). *JRC Data Cat*.

Qian, Y., Chakraborty, T. C., Li, J., Li, D., He, C., Sarangi, C., Chen, F., Yang, X., & Leung, L. R. (2022). Urbanization Impact on Regional Climate and Extreme Weather: Current Understanding, Uncertainties, and Future Research Directions. *Advances in Atmospheric Sciences*. https://doi.org/10.1007/s00376-021-1371-9

Raymond, C., Matthews, T., & Horton, R. M. (2020). The emergence of heat and humidity too severe for human tolerance. *Science Advances*, *6*(19), eaaw1838. https://doi.org/10.1126/sciadv.aaw1838

Remme, R. P., Frumkin, H., Guerry, A. D., King, A. C., Mandle, L., Sarabu, C., Bratman, G. N., Giles-Corti, B., Hamel, P., Han, B., Hicks, J. L., James, P., Lawler, J. J., Lindahl, T., Liu, H., Lu, Y., Oosterbroek, B., Paudel, B., Sallis, J. F., … Daily, G. C. (2021). An ecosystem service perspective on urban nature, physical activity, and health. *Proceedings of the National Academy of Sciences*, *118*(22), e2018472118. https://doi.org/10.1073/pnas.2018472118

Rothfusz, L. P., & Headquarters, N. S. R. (1990). The heat index equation (or, more than you ever wanted to know about heat index). *Fort Worth, Texas: National Oceanic and Atmospheric Administration, National Weather Service, Office of Meteorology*, *9023*.

Rouse, J. W., Haas, R. H., Schell, J. A., Deering, D. W., & Harlan, J. C. (1974). Monitoring the vernal advancement and retrogradation (green wave effect) of natural vegetation. *NASA/GSFC Type III Final Report, Greenbelt, Md*, *371*.

Sarangi, C., Qian, Y., Li, J., Leung, L. R., Chakraborty, T. C., & Liu, Y. (2021). Urbanization Amplifies Nighttime Heat Stress on Warmer Days Over the US. *Geophysical Research Letters*, *48*(24). https://doi.org/10.1029/2021GL095678

Schwaab, J., Meier, R., Mussetti, G., Seneviratne, S., Bürgi, C., & Davin, E. L. (2021). The role of urban trees in reducing land surface temperatures in European cities. *Nature Communications*, *12*(1), 1–11.

Sharma, A., Wuebbles, D. J., & Kotamarthi, R. (2021). The Need for Urban-Resolving Climate Modeling Across Scales. *AGU Advances*, *2*(1). https://doi.org/10.1029/2020AV000271

Sherwood, S. C. (2018). How Important Is Humidity in Heat Stress? *Journal of Geophysical Research: Atmospheres*, *123*(21). https://doi.org/10.1029/2018JD028969

Sherwood, S. C., & Huber, M. (2010). An adaptability limit to climate change due to heat stress. *Proceedings of the National Academy of Sciences*, *107*(21), 9552–9555. https://doi.org/10.1073/pnas.0913352107

Steadman, R. G. (1979). The assessment of sultriness. Part I: A temperature-humidity index based on human physiology and clothing science. *Journal of Applied Meteorology and Climatology*, *18*(7), 861–873.

Stone Jr, B., Lanza, K., Mallen, E., Vargo, J., & Russell, A. (2019). Urban heat management in Louisville, Kentucky: A framework for climate adaptation planning. *Journal of Planning Education and Research*, 0739456X19879214.

Stull, R. (2011). Wet-Bulb Temperature from Relative Humidity and Air Temperature. *Journal of Applied Meteorology and Climatology*, *50*(11), 2267–2269. https://doi.org/10.1175/JAMC-D-11-0143.1

Venter, Z. S., Chakraborty, T., & Lee, X. (2021). Crowdsourced air temperatures contrast satellite measures of the urban heat island and its mechanisms. *Science Advances*, *7*(22), eabb9569. https://doi.org/10.1126/sciadv.abb9569

Wan, Z. (2006). MODIS land surface temperature products users' guide. *Institute for Computational Earth System Science, University of California: Santa Barbara, CA, USA*, *805*.

Wang, W., Chakraborty, T. C., Xiao, W., & Lee, X. (2021). Ocean surface energy balance allows a constraint on the sensitivity of precipitation to global warming. *Nature Communications*, *12*(1), 2115. https://doi.org/10.1038/s41467-021-22406-7

Wang, Z., Song, J., Chan, P. W., & Li, Y. (2021). The urban moisture island phenomenon and its mechanisms in a high-rise high-density city. *International Journal of Climatology*, *41*(S1). https://doi.org/10.1002/joc.6672

Wilcoxon, F., Kotz, S., & Johnson, N. L. (1992). Breakthroughs in Statistics: Methodology and Distribution. *New York, NY: Springer New York*, 196–2.

Wong, N. H., Tan, C. L., Kolokotsa, D. D., & Takebayashi, H. (2021). Greenery as a mitigation and adaptation strategy to urban heat. *Nature Reviews Earth & Environment*, *2*(3), 166–181. https://doi.org/10.1038/s43017-020-00129-5

Zhang, P., Bounoua, L., Imhoff, M. L., Wolfe, R. E., & Thome, K. (2014). Comparison of MODIS land surface temperature and air temperature over the continental USA meteorological stations. *Canadian Journal of Remote Sensing*, *40*(2), 110–122.

Zhao, L., Lee, X., & Schultz, N. M. (2017). A wedge strategy for mitigation of urban warming in future climate scenarios. *Atmospheric Chemistry and Physics*, *17*(14), 9067–9080. https://doi.org/10.5194/acp-17-9067-2017

Zhao, L., Lee, X., Smith, R. B., & Oleson, K. (2014). Strong contributions of local background climate to urban heat islands. *Nature*, *511*(7508), 216–219.

Zhao, L., Oleson, K., Bou-Zeid, E., Krayenhoff, E. S., Bray, A., Zhu, Q., Zheng, Z., Chen, C., & Oppenheimer, M. (2021). Global multi-model projections of local urban climates. *Nature Climate Change*, *11*(2), 152–157. https://doi.org/10.1038/s41558-020-00958-8

Zhao, Q., Yang, J., Wang, Z.-H., & Wentz, E. A. (2018). Assessing the cooling benefits of tree shade by an outdoor urban physical scale model at Tempe, AZ. *Urban Science*, *2*(1), 4.

Zheng, Z., Zhao, L., & Oleson, K. W. (2021). Large model structural uncertainty in global projections of urban heat waves. *Nature Communications*, *12*(1), 1–9.

Ziter, C. D., Pedersen, E. J., Kucharik, C. J., & Turner, M. G. (2019). Scale-dependent interactions between tree canopy cover and impervious surfaces reduce daytime urban heat during summer. *Proceedings of the National Academy of Sciences*, *116*(15), 7575–7580. https://doi.org/10.1073/pnas.1817561116

Supplementary Materials: Lower urban humidity moderates heat stress

T. Chakraborty[1,3,*], Z. S. Venter[2], Y. Qian[3], X. Lee[1,*]

[1]School of the Environment, Yale University, New Haven, CT, USA

[2]Terrestrial Ecology Section, Norwegian Institute for Nature Research—NINA, 0349 Oslo, Norway

[3]Pacific Northwest National Laboratory, Richland, WA, USA

Corresponding Authors: T. Chakraborty (tc.chakraborty@pnnl.gov) and X. Lee (xuhui.lee@yale.edu)

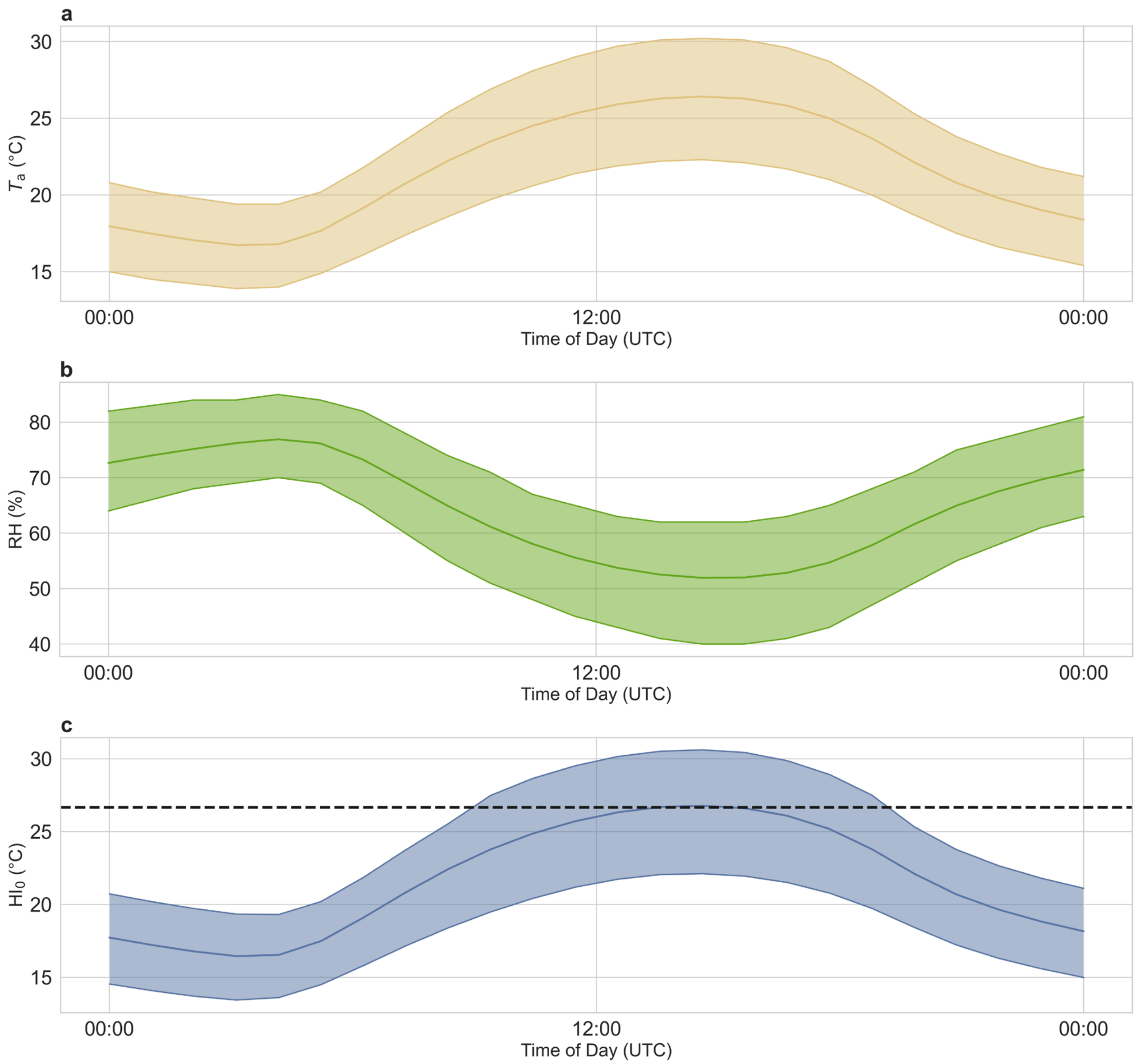

Fig. S1 Diurnal composites of citizen weather station data. Diurnal composites of Netatmo **a** air temperature (T_a), **b** relative humidity (RH), and **c** heat index (HI_0) from all stations in rural buffers considered in the present study. The upper and lower lines represent the 75% and 25% percentile of the measurements, and the middle line is for the mean from all the observations by hour of the day. The dashed horizontal line in sub-figure **c** shows the threshold below which the simplified equation is used for calculating HI_0 (Eq. 1 in Methods).

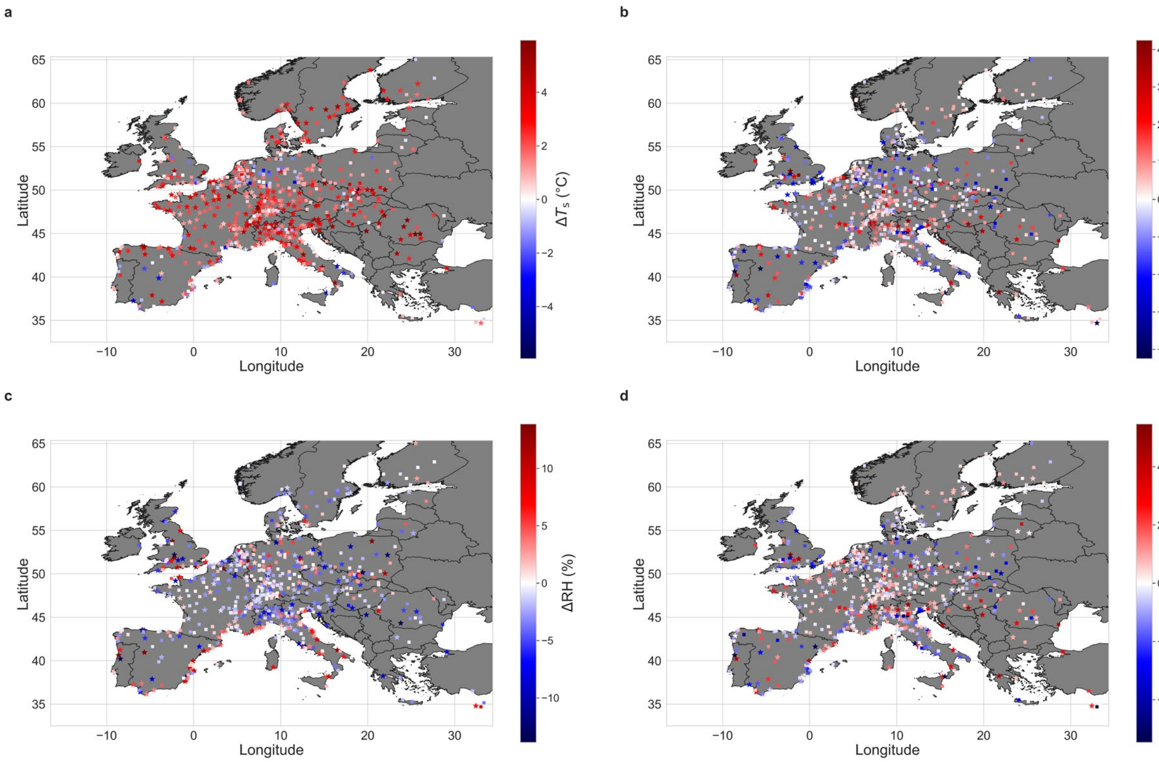

Fig. S2 Urban-rural differences for Terra day across urban clusters in Europe. Spatial distribution of urban-rural differences in **a** surface temperature (ΔT_{s}), **b** air temperature (ΔT_{a}), **c** relative humidity (ΔRH), and **d** heat index ($\Delta \mathrm{HI}_0$) for urban clusters in Europe with sufficient data corresponding to the Terra satellite daytime overpass (≈10:30 am local time) for July 2019. The stars represent clusters with statistically significant (p<0.01) differences between the urban and rural values.

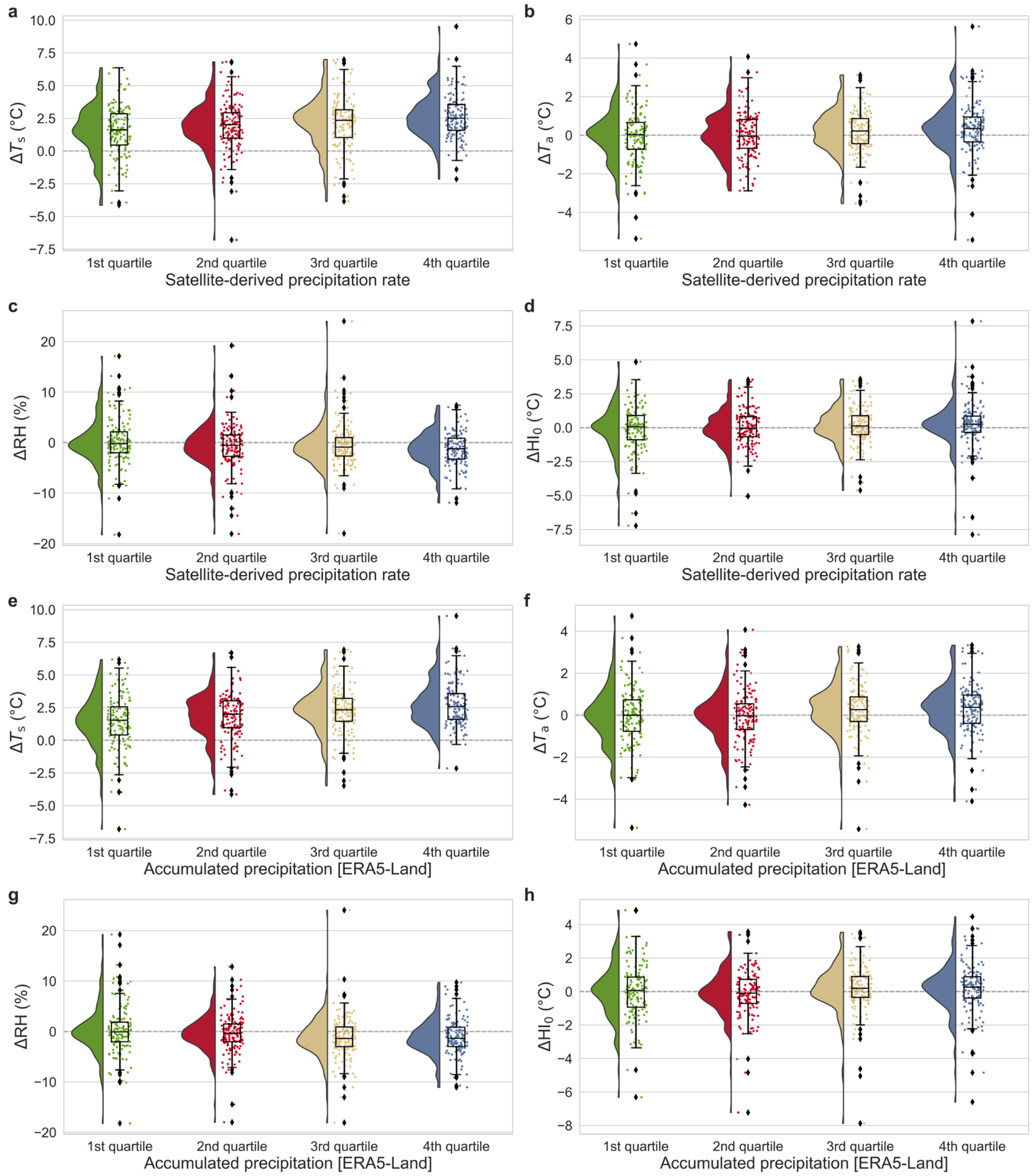

Fig. S3 Urban-rural differences in variables for precipitation quartiles. Distributions of urban-rural differences in **a** surface temperature (ΔT_s), **b** air temperature (ΔT_a), **c** relative humidity (ΔRH), and **d** heat index (ΔHI_0) corresponding to the Aqua daytime overpass (≈1:30 pm local time) for quartiles of satellite-derived precipitation rate in July 2019. Sub-figures **e**, **f**, **g**, and **h** are similar, but use quartiles of accumulation precipitation in July 2019 from the ERA5-Land reanalysis dataset.

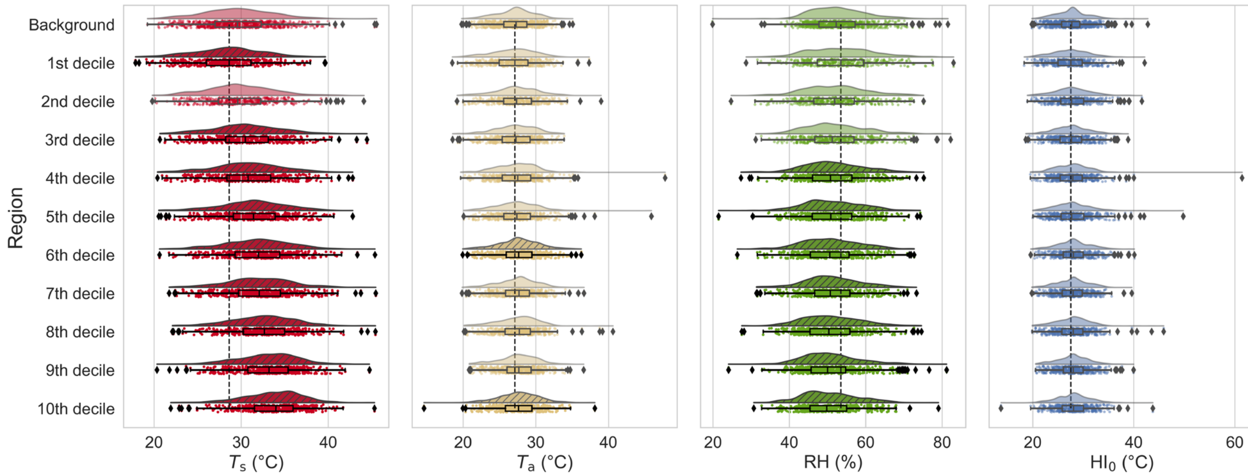

Fig. S4 Intra-urban gradients of variables for Terra day. Distributions of composite mean surface temperature (T_s), air temperature (T_a), relative humidity (RH), and heat index (HI_0) in each of the T_s decile neighborhoods across the urban clusters considered. The vertical dashed lines mark the median of the distribution of the corresponding variable in the 1st T_s decile neighborhood. Decile neighborhoods that show statistically significant ($p<0.01$) differences from the background reference values are shown using hatched density plots and darker shades. All calculations are for the Terra daytime overpass (≈10:30 am local time) for July 2019.

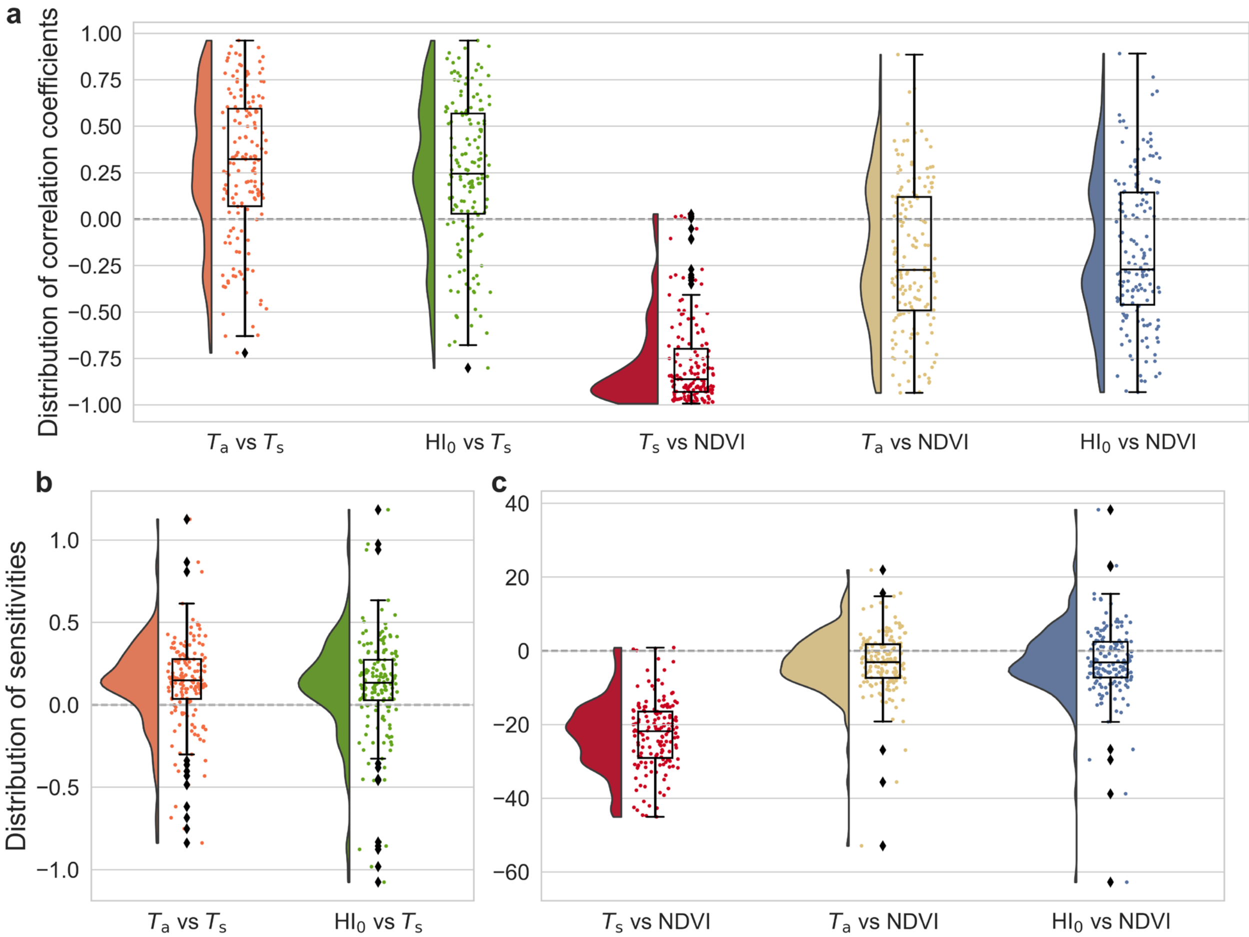

Fig. S5 Associations between variables within urban clusters for Terra day. Sub-fig **a** shows the distributions of the correlation coefficient (*r*) of linear regressions between surface temperature (T_s) and air temperature (T_a), T_s and heat index (HI_0), Normalized Difference Vegetation Index (NDVI) and T_s, NDVI and T_a, and NDVI and HI_0, respectively, for urban clusters in Europe. Each data point is from a linear regression between pairs of variables for a cluster. The linear regressions have a sample size of ten (one for each T_s decile neighborhood). Sub-fig **b** and **c** show the distributions of the slope of those linear regressions, or the sensitivity of one variable to unit changes in the other. The unit of sensitivity in Sub-fig **c** is °C per unit NDVI. All calculations are for the Terra daytime overpass (≈10:30 am local time) for July 2019.

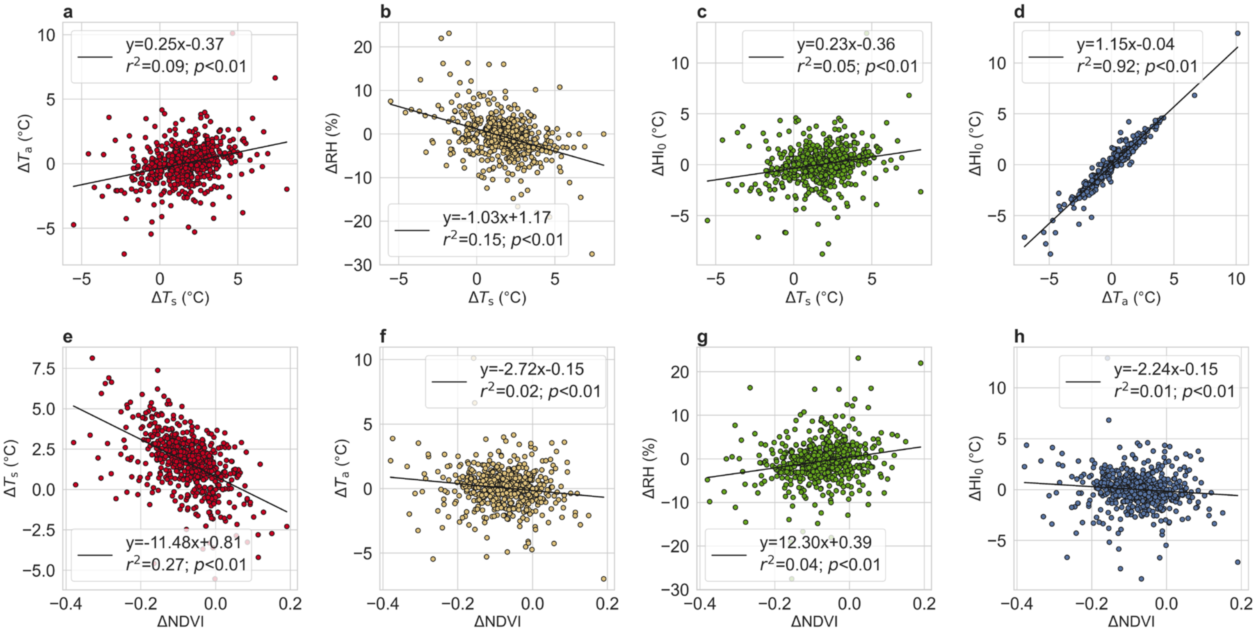

Fig. S6 Associations between variables across urban clusters for Terra day. Associations between urban-rural differences in **a** surface temperature (ΔT_s) and air temperature (ΔT_a), **b** ΔT_s and relative humidity (ΔRH), **c** ΔT_s and heat index (ΔHI_0), **d** ΔT_a and ΔHI_0, **e** Normalized Difference Vegetation Index (ΔNDVI) and ΔT_s, **f** ΔNDVI and ΔT_a, **g** ΔNDVI and ΔRH, and **h** ΔNDVI and ΔHI_0 across urban clusters in Europe. Each dot represents one cluster and the lines and equations of best fit are shown. All calculations are for the Terra daytime overpass (≈10:30 pm local time) for July 2019.

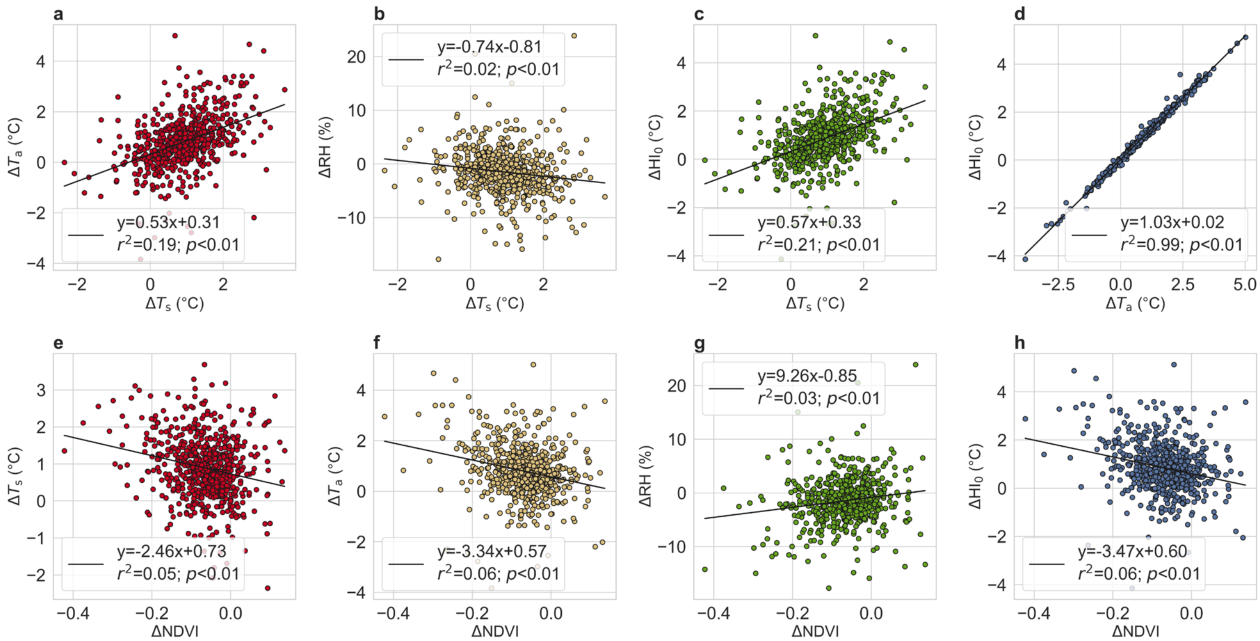

Fig. S7 Associations between variables across urban clusters for Aqua night. Associations between urban-rural differences in **a** surface temperature (ΔT_s) and air temperature (ΔT_a), **b** ΔT_s and relative humidity (ΔRH), **c** ΔT_s and heat index (ΔHI_0), **d** ΔT_a and ΔHI_0, **e** Normalized Difference Vegetation Index (ΔNDVI) and ΔT_s, **f** ΔNDVI and ΔT_a, **g** ΔNDVI and ΔRH, and **h** ΔNDVI and ΔHI_0 across urban clusters in Europe. Each dot represents one cluster and the lines and equations of best fit are shown. All calculations are for the Aqua nighttime overpass (≈1:30 am local time) for July 2019.

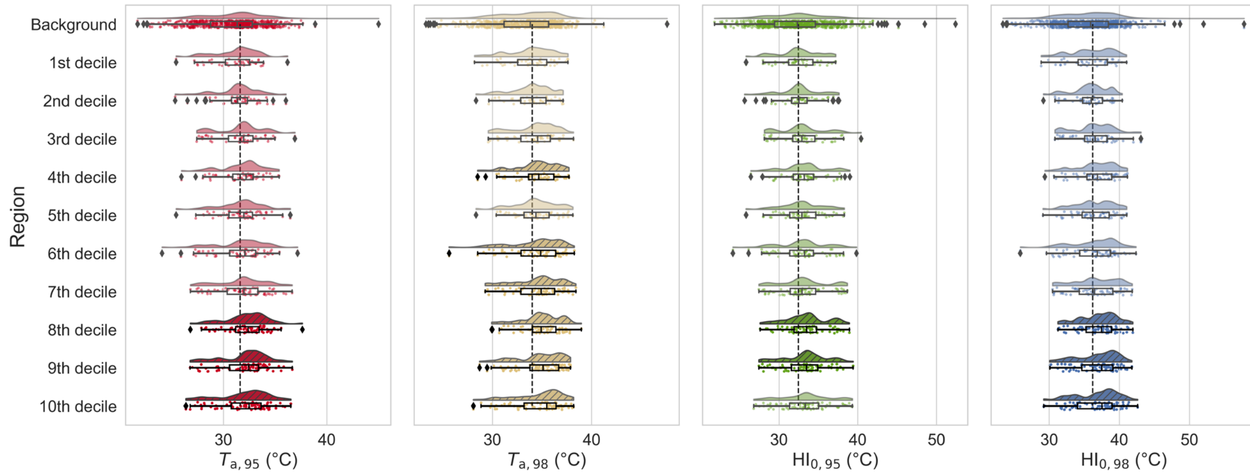

Fig. S8 Intra-urban gradients of extremes. Distributions of the 95th and 98th percentile of hourly observations in July 2019 of air temperature (T_a) and heat index (HI_0) in each of the T_s decile neighborhoods across the urban clusters considered. The vertical dashed lines mark the median of the distribution of the corresponding variable in the 1st T_s decile neighborhood. Decile neighborhoods that show statistically significant ($p<0.01$) differences from the background reference values are shown using hatched density plots and darker shades.

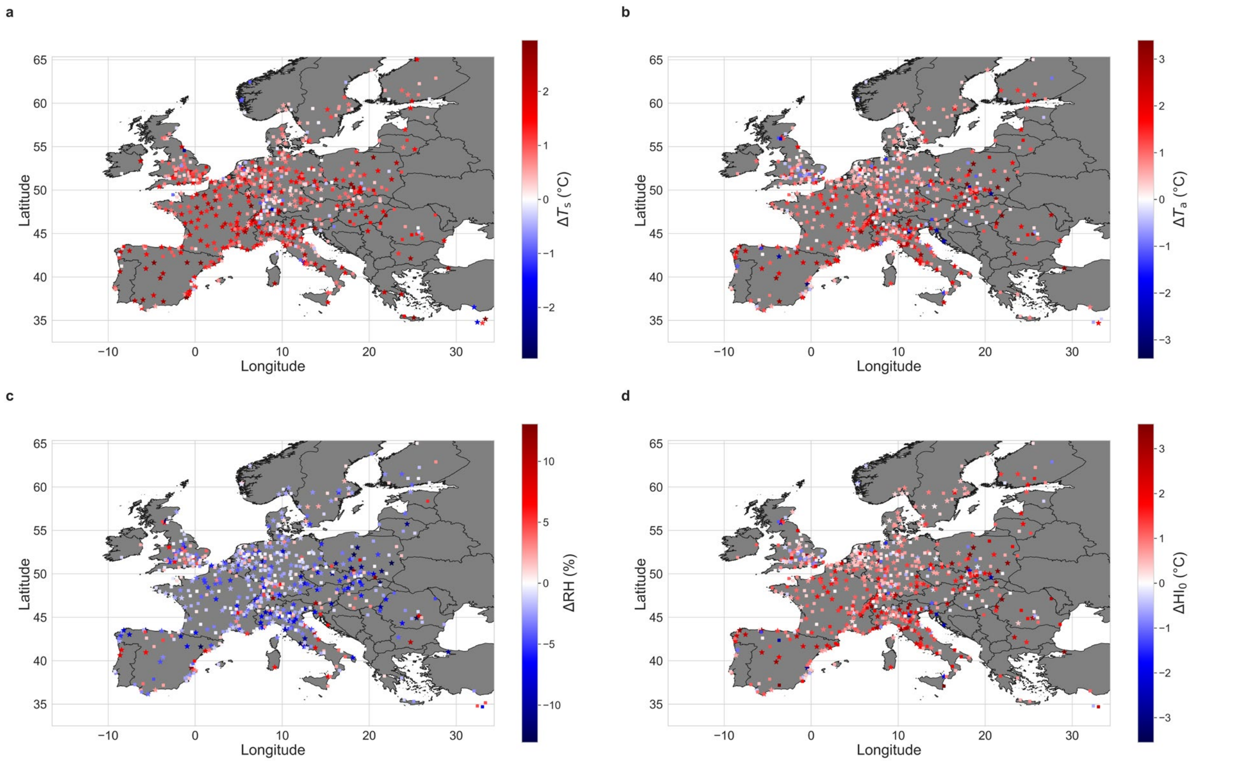

Fig. S9 Urban-rural differences for Aqua night across urban clusters in Europe. Spatial distribution of urban-rural differences in **a** surface temperature (ΔT_s), **b** air temperature (ΔT_a), **c** relative humidity (ΔRH), and **d** heat index (ΔHI_0) for urban clusters in Europe with sufficient data corresponding to the Aqua satellite nighttime overpass (≈1:30 am local time) for July 2019. The stars represent clusters with statistically significant ($p<0.01$) differences between the urban and rural values.

Table S1. P-values of the Mann –Whitney two-sample statistic between the observations corresponding to the Aqua daytime overpass (≈1:30 pm local time) in the background reference region and the observations in the decile neighborhoods for surface temperature (T_s), air temperature (T_a), relative humidity (RH), US National Weather Service heat index (HI_0), four additional estimates of heat index (HI_1 to HI_4), and the humidex for July 2019.

Group	T_s	T_a	RH	HI_0	HI_1	HI_2	HI_3	HI_4	Humidex
1st decile	<0.01	0.16	0.25	0.26	0.21	0.24	0.21	0.18	0.23
2nd decile	0.25	0.23	0.06	0.25	0.27	0.25	0.32	0.23	0.39
3rd decile	0.01	0.43	0.38	0.39	0.40	0.38	0.42	0.41	0.46
4th decile	<0.0001	0.38	<0.01	0.74	0.72	0.74	0.94	0.43	0.91
5th decile	<0.0001	0.09	<0.01	0.25	0.23	0.24	0.34	0.1	0.43
6th decile	<0.0001	0.01	<0.01	0.05	0.05	0.05	0.09	0.02	0.14
7th decile	<0.0001	0.02	<0.0001	0.13	0.11	0.13	0.24	0.03	0.37
8th decile	<0.0001	<0.01	<0.0001	0.05	0.04	0.05	0.11	<0.01	0.20
9th decile	<0.0001	<0.0001	<0.0001	<0.001	<0.001	<0.001	<0.01	<0.0001	<0.01
10th decile	<0.0001	<0.0001	<0.0001	<0.01	<0.01	<0.01	<0.01	<0.0001	0.03

Table S2. P-values of the Mann –Whitney two-sample statistic between the observations corresponding to the Terra daytime overpass (≈10:30 am local time) in the background reference region and the observations in the decile neighborhoods for surface temperature (T_s), air temperature (T_a), relative humidity (RH), US National Weather Service heat index (HI_0), four estimates of heat index (HI_1 to HI_4), and the humidex for July 2019.

Group	T_s	T_a	RH	HI_0	HI_1	HI_2	HI_3	HI_4	Humidex
1st decile	<0.0001	0.27	0.27	0.25	0.27	0.29	0.26	0.28	0.25
2nd decile	0.49	0.41	0.08	0.55	0.58	0.49	0.70	0.44	0.80
3rd decile	<0.001	0.85	0.06	0.86	0.82	0.89	0.60	0.91	0.49
4th decile	<0.0001	0.28	<0.01	0.50	0.58	0.48	0.81	0.32	0.98
5th decile	<0.0001	0.44	<0.001	0.81	0.86	0.74	0.85	0.52	0.70
6th decile	<0.0001	<0.01	<0.0001	0.04	0.04	0.04	0.09	<0.01	0.16
7th decile	<0.0001	0.05	<0.001	0.15	0.17	0.14	0.33	0.07	0.49
8th decile	<0.0001	0.03	<0.0001	0.13	0.14	0.12	0.31	0.04	0.47
9th decile	<0.0001	0.01	<0.0001	0.06	0.07	0.06	0.18	0.02	0.29
10th decile	<0.0001	<0.01	<0.0001	0.03	0.04	0.02	0.09	<0.01	0.16

Table S3. P-values of the Mann –Whitney two-sample statistic between the 95th and 98th percentile of hourly observations in July 2019 of air temperature (T_a) and US National Weather Service heat index (HI_0) for CWSs in the background reference region and the corresponding observations in the decile neighborhoods.

Group	$T_{a,95}$	$T_{a,98}$	$HI_{0,95}$	$HI_{0,98}$
1st decile	0.48	0.36	0.63	0.41
2nd decile	0.40	0.34	0.54	0.69
3rd decile	0.06	0.05	0.15	0.18
4th decile	0.01	<0.01	0.04	0.02
5th decile	0.05	0.03	0.13	0.11
6th decile	0.03	<0.01	0.11	0.06
7th decile	0.01	<0.01	0.06	0.03
8th decile	<0.001	<0.0001	<0.01	<0.01
9th decile	<0.001	<0.0001	<0.01	<0.01
10th decile	<0.001	<0.0001	0.01	<0.01

Table S4. P-values of the Mann –Whitney two-sample statistic between the observations corresponding to the Aqua nighttime overpass (≈1:30 am local time) in the background reference region and the observations in the decile neighborhoods for surface temperature (T_s), air temperature (T_a), relative humidity (RH), US National Weather Service heat index (HI_0), four additional estimates of heat index (HI_1 to HI_4), and the humidex for July 2019.

Group	T_s	T_a	RH	HI_0	HI_1	HI_2	HI_3	HI_4	Humidex
1st decile	<0.0001	0.27	0.12	0.21	0.21	0.20	0.16	0.26	0.14
2nd decile	0.14	0.42	0.01	0.46	0.48	0.30	0.57	0.43	0.61
3rd decile	0.79	0.15	<0.01	0.18	0.18	0.21	0.25	0.16	0.28
4th decile	0.01	0.02	<0.01	0.02	0.02	0.56	0.02	0.02	0.03
5th decile	<0.001	0.01	<0.01	0.01	0.01	0.38	0.02	0.01	0.02
6th decile	<0.0001	<0.0001	<0.0001	<0.0001	<0.0001	0.45	<0.0001	<0.0001	<0.0001
7th decile	<0.0001	<0.0001	<0.0001	<0.0001	<0.0001	0.63	<0.0001	<0.0001	<0.0001
8th decile	<0.0001	<0.0001	<0.0001	<0.0001	<0.0001	0.56	<0.0001	<0.0001	<0.0001
9th decile	<0.0001	<0.0001	<0.0001	<0.0001	<0.0001	0.47	<0.0001	<0.0001	<0.0001
10th decile	<0.0001	<0.0001	<0.0001	<0.0001	<0.0001	0.02	<0.0001	<0.0001	<0.0001